Supplement of

Development, Characterization and Rapid Diagnostics of an Aircraft Aerosol Mass Spectrometer Inlet System

5 **Dongwook Kim et al.,**

Correspondence to: Jose L. Jimenez (jose.jimenez@colorado.edu)

Supporting Information

S1. Small particle generation system

It is challenging to generate small monodisperse particles with the typical combination of a nebulizer and DMA-impactor system (TSI Inc.) which is not suitable for removing multiply charged particles below 150 nm d_m range. An evaporation-condensation system was used instead to generate monodisperse oleic acid particles for the characterization of the transmission efficiency in the 30-300 nm d_{va} range with minimal interference from multiply charged particles. Briefly, Zero Air (ZA) flows into a hot glass bulb containing oleic acid and then carries oleic acid vapor (heated flow). Evaporated oleic acid vapor inside the heated bath is mixed with zero air (quenching flow) via a glass "Y" and quenched going through a mixing tube, resulting in condensation of oleic acid and particle formation and growth (Fig. S1a). In the system used in this study, an additional heater was added to the evaporation-condensation system used by Krechmer et al. (2017) and Hu et al. (2018b) to fully encapsulate the glass bulb for homogeneous heating and minimize perturbations by temperature variations in the laboratory. The heat/quenching flows and the temperature of the heat bath determine the particle size distribution of oleic acid downstream of the evaporation-condensation system. The flows and temperatures were optimized for particle generation below 300 nm d_m by monitoring the particle size distribution using a scanning mobility particle sizer (SMPS) (Fig. S1b). Then the differential mobility analyzer (DMA) downstream of the small particle generator was used to select a particle size (larger than the peak diameter of the monomodal distribution) to minimize the population of doubly charged particles in the output (Fig. S1c). The monodispersity of the particle size distribution downstream of the DMA was routinely confirmed using AMS ePToF measurements (Fig. S2).
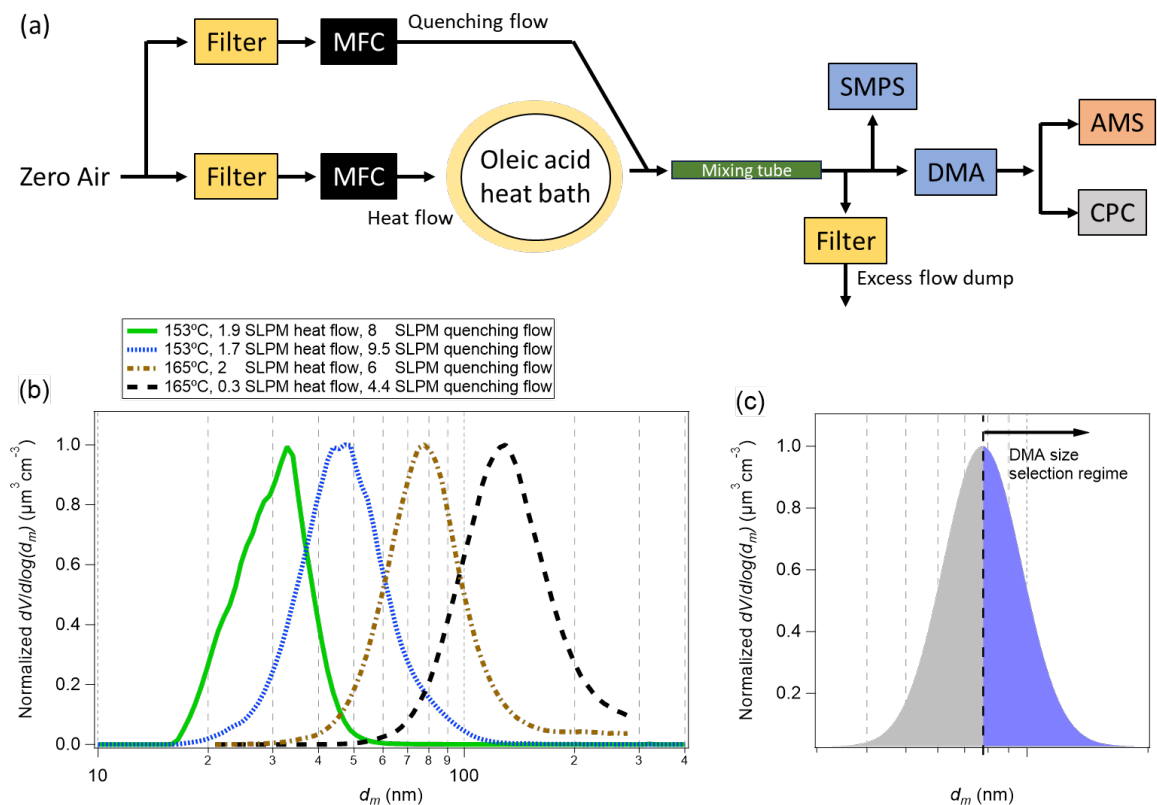
Figure S1.1: (a) Evaporation-condensation system modified for small particle generation. (b) Oleic acid volume size distributions measured by SMPS generated from the evaporation-condensation system at different temperatures, heat flow, and quenching flow setups. Although the system's response to temperature and flows was highly nonlinear, higher temperature and lower heat flow yielded larger particles. The selected DMA sizes were larger than the peak diameter to minimize the population of doubly charged particles (c).

70
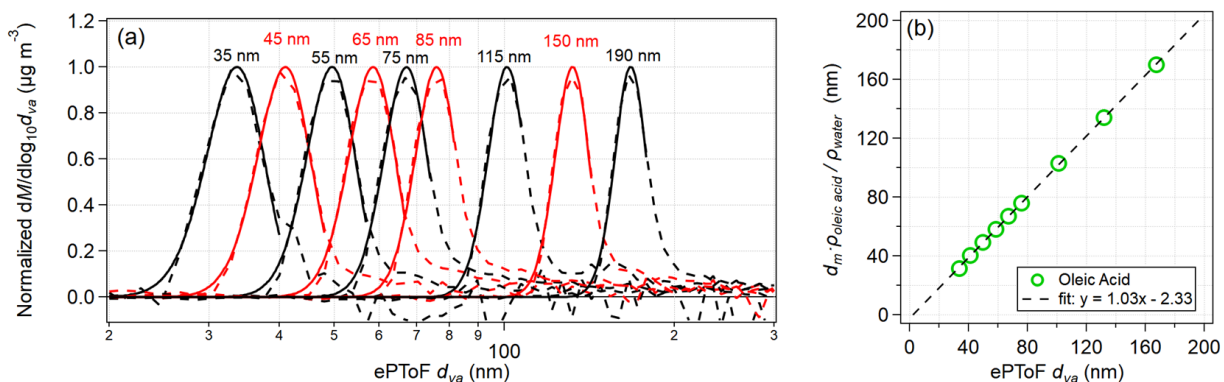
Figure S1.2. (a) Particle size distributions of the monodisperse oleic acid particles measured by ePToF (dotted lines). The diameters denoted above the distributions are the mobility diameters selected by the DMA. The mean ePToF d_{va} was determined by fitting with the Gaussian function (solid line). The fitting range was selected so that fitting the tailing on the right shoulder is avoided. The tailing effect is due to the prolonged evaporation especially when the input aerosol concentration is high. (b) The nominal d_{va} ($d_m \cdot \rho_{oleic\ acid} / \rho_{water}$) vs measured d_{va} using ePToF of the monodisperse oleic acid particles. $\rho_{oleic\ acid} / \rho_{water}$ is 0.895. These are the data used for ePToF calibration of the PM_1 lens in Fig. 14d.
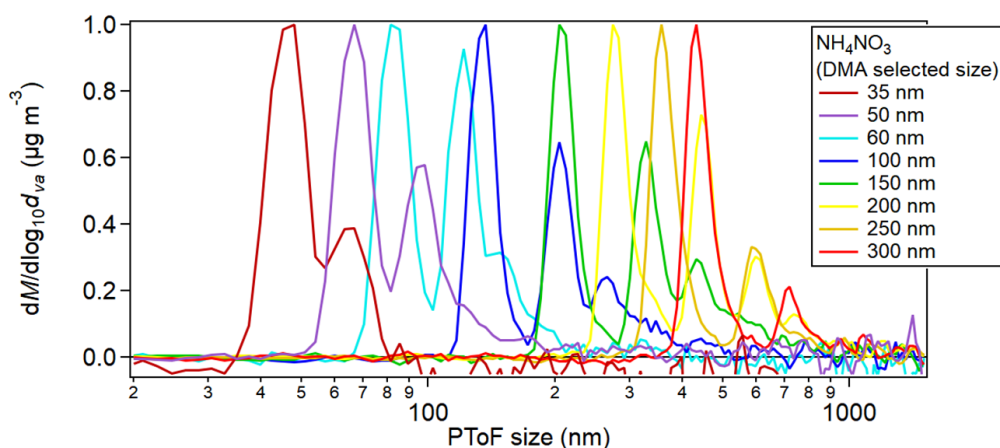
Figure S1.3. AMS PToF distribution of NH_4NO_3 particles used for monodisperse BWP in Fig. 9. These were generated with a TSI atomizer and DMA without an impactor, hence multiply charged particles were present.

S2. Measurement of CPC dilution factor
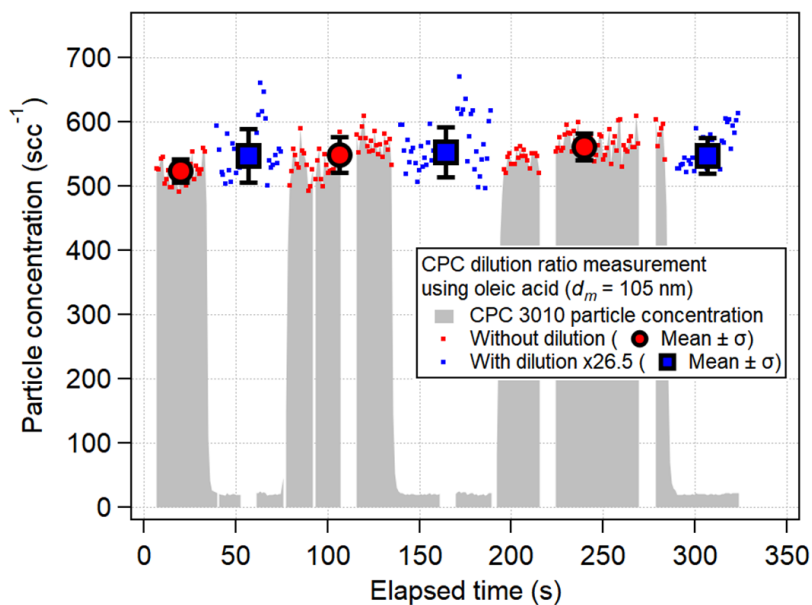
Figure S2.1. An example of particle dilution factor measurement of the particle dilution system in front of CPC 3010 (Fig.1) using 105 nm d_m oleic acid particles. The gray area indicates the measured particle counts while the dilution system is turned on and off. The red dots and markers are the particle concentrations without dilution and the blue dots and markers are particle counts multiplied by the dilution factor (26.5) during particle dilution. The dilution factor is the scaling factor applied to the diluted particle counts to match the undiluted particle counts. Measured dilution ratios were within the 25-27 range.

S3. Particle loss in the sampling lines upstream of ADL
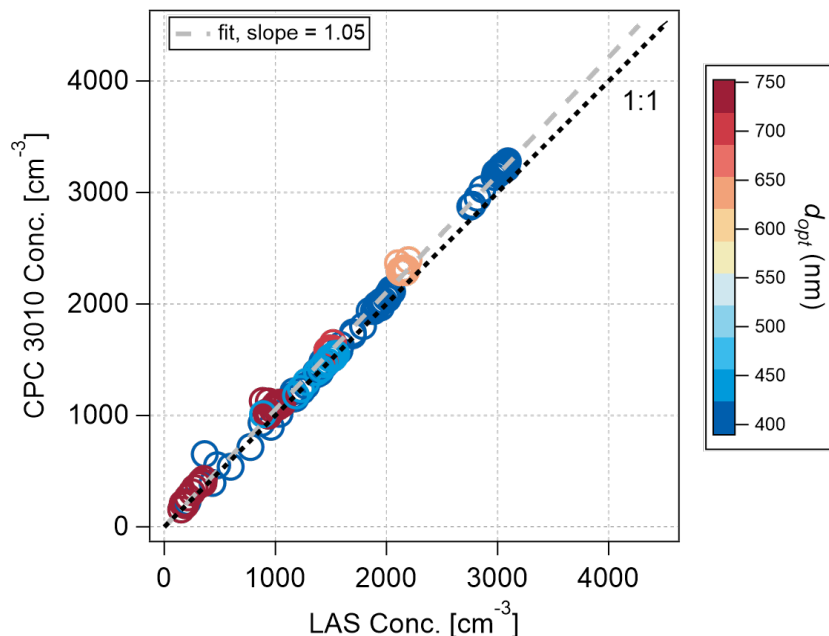
Figure S3.1. Scatter plot of particle concentrations from CPC 3010 and Laser aerosol spectrometer (LAS, TSI Inc.) using multiple PSL sizes. The data are colored by the optical diameter measured by the LAS. This comparison was performed to assess the particle losses in the sampling/dilution line between the AMS inlet and the CPC. The LAS was teed into the AMS inlet line (Fig. 1). If there were significant particle losses in the sampling line to the CPC, the losses of large particles would be more pronounced due to higher impaction losses. The absence of a systematic low bias for the CPC counts (especially the larger particles) indicates that the particle losses in the sampling line between CPC and AMS are negligible for submicron particles.
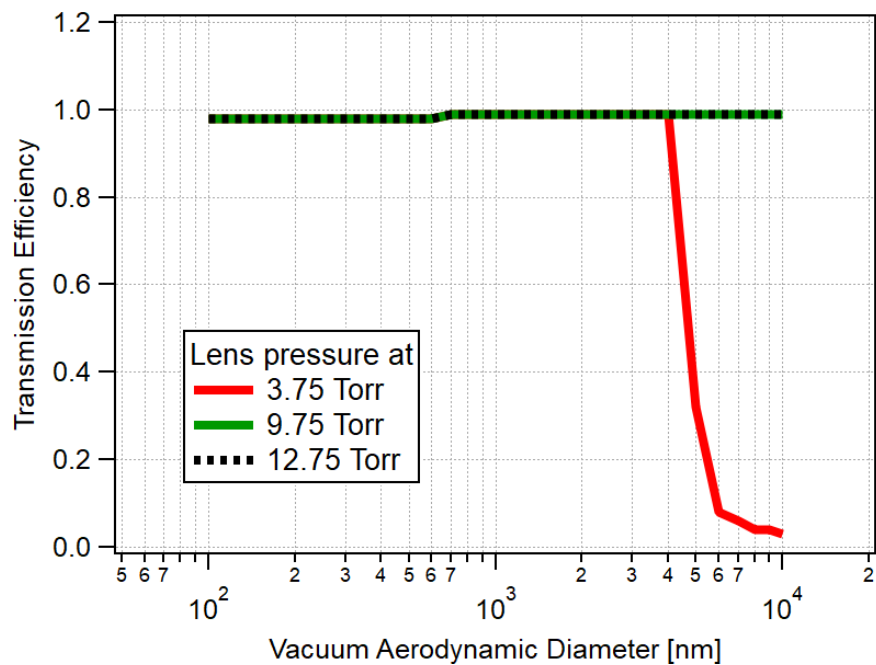
Figure S3.2. CFD modeling of particle transmission efficiency of the expansion volume version C (EV-C) with 120 μm critical orifice.

S4. Determination of the Jayne shape factor (S), E_b, and RIE of test aerosols

In this study, oleic acid, NH_4NO_3, $(NH_4)_2SO_4$, and NH_4I were used to measure inlet transmission efficiencies. Quantification of NH_4NO_3 particles, extensively used for ionization efficiency calibration of AMS, is straightforward since it fully evaporates on the surface of the vaporizer without bouncing ($E_b = 1$). The Jayne shape factor (S) of NH_4NO_3 is known to be 0.8 (Jayne et al., 2000). Thus, the transmission measurements with NH_4NO_3 particles serve as reference and the parameters for quantification of other test aerosols (S, E_b) were derived in comparison to the measurements with NH_4NO and listed in Table S4.1. S of NH_4I and $(NH_4)_2SO_4$ were determined by comparing with the measured d_{va} by AMS (ePToF d_{va}) following Eq. 5 (Fig. S4.1a and c). $1/E_b$ of NH_4I and $(NH_4)_2SO_4$ is the scaling factor applied to match the transmission efficiency with NH_4I and $(NH_4)_2SO_4$ to the transmission efficiency measured with NH_4NO_3 (Fig. S4.1b and d). RIEs of I^- and SO_4^{2-} were measured relative to NH_4^+. E_b of oleic acid is 1 (Alfarra, 2004; Matthew et al., 2008). RIE of oleic acid is assigned so that the transmission efficiency is ~ 1 over the d_{va} range where E_L or $TE = 1$ (Fig. S4.1e). The measured values of E_b, RIE, and S in this work are summarized in Table S4.1 and Fig. S4.2. The measured RIE of oleic acid (3.58 ± 0.39) is within previously reported values, 3.0 (Xu et al., 2018), 3.18 ± 0.95 (Katz et al., 2021), and 3.94 (Nault et al., 2023).
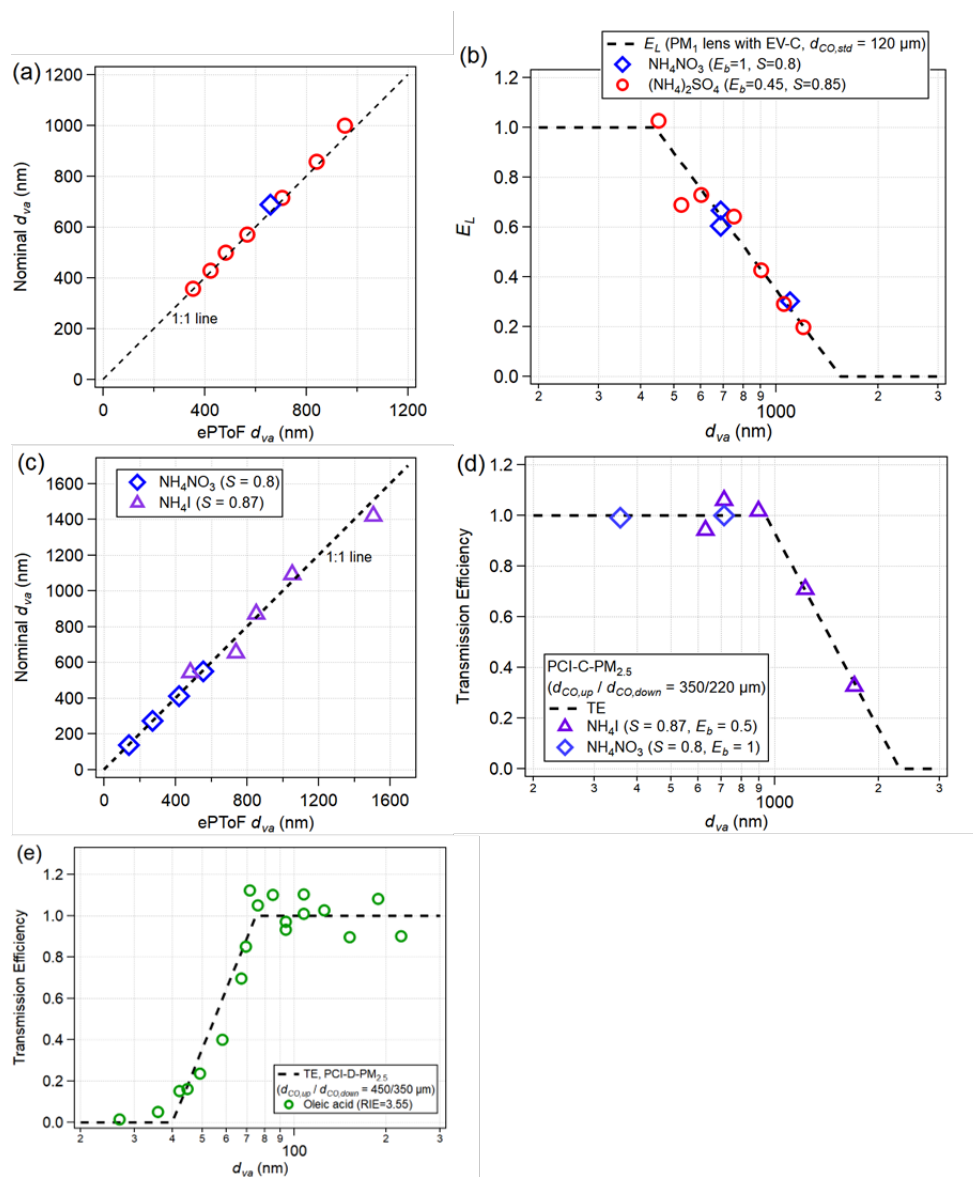
Figure S4.1. Examples of determination of the bouncing term of transmission efficiency (E_b), Jayne shape factor (S), and relative ionization efficiency (RIE) of the test aerosols. (a) Zoomed-in Fig. 14a on the large particle transmission and the data points are specified by the components. (b) The E_b of $(NH_4)_2SO_4$ particles were determined by scaling to the NH_4NO_3 particles. This specific case showed higher E_b for $(NH_4)_2SO_4$ than normal values (Fig. S4.2). (c) S of NH_4I was determined by measuring the d_{va} of test aerosols with ePToF and comparing them with the nominal d_{va} (= bulk density (ρ_{bulk})·d_m·S). (d) The E_b of NH_4I was determined using the same method as in (b). (e) Determination of oleic acid RIE. The application of RIE$_{oleic\ acid}$ = 3.55 achieved the plateau at TE ~ 1 over d_{va} > 80 nm which is considered beyond the partial transmission region.

135 **Table S4.1.** The bulk density (ρ_{bulk}), Jayne shape factor (S), collection efficiency that accounts for particle bouncing at the vaporizer (E_b), and relative ionization efficiency (RIE) of test aerosols. The E_b and RIE of PSL were not investigated because PSL was only used for PToF particle size calibration purposes where E_b and RIE are not needed. The RIE of NH_4^+ is determined by comparison of NO_3^- mass in NH_4NO_3 particles. Once the RIE of NH_4 is determined, RIEs of I^- and SO_4^{2-} are determined by comparing to NH_4^+ mass in NH_4I and $(NH_4)_2SO_4$ particles. Error bars indicate the standard deviation of measured values. E_b

140 of dry $(NH_4)_2SO_4$ particles reported in this study is consistent with other studies, *e.g.*, 0.25–0.5 (2008), 0.4–0.5 (Hu et al., 2017) and 0.37 ± 0.13 (Day et al., 2022). Note that S of dry $(NH_4)_2SO_4$ particles is typically assumed to be 1 when estimating E_b from mass based comparison between AMS and CPC, in which case the reported E_b is $E_b \cdot S$. In this study, S was measured with from ePToF (Fig. S4.1) and applied to Eq. 10 when estimating E_b from AMS and CPC mass comparison.

Compound	ρ_{bulk} (g cm^{-3})	S	E_b	RIE
PSL	1.055	1	-	-
Oleic acid	0.895	1	1	3.58 ± 0.39 (OA*)
NH_4NO_3	1.72	0.8	1	-
$(NH_4)_2SO_4$	1.77	0.83 ± 0.05	$0.35 \pm 0.06^*$	1.38 ± 0.01 (SO_4^{2-})
NH_4I	2.51	0.82 ± 0.07	0.54 ± 0.15	0.79 ± 0.19 (I^-)
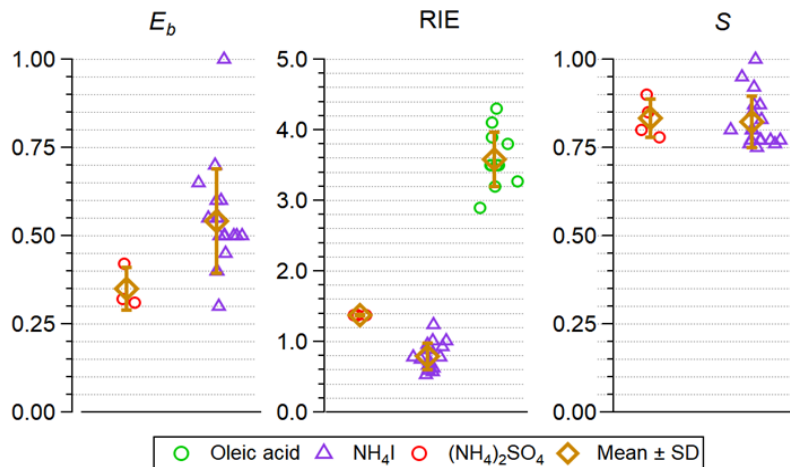
145

Figure S4.2. The E_b RIE and S data are measured with three ADLs (PM$_1$, PM$_{2.5}$ lens, and HPL), with and without PCI, and with two standard vaporizers. The mean values ± standard deviation are listed in Table S4.1.
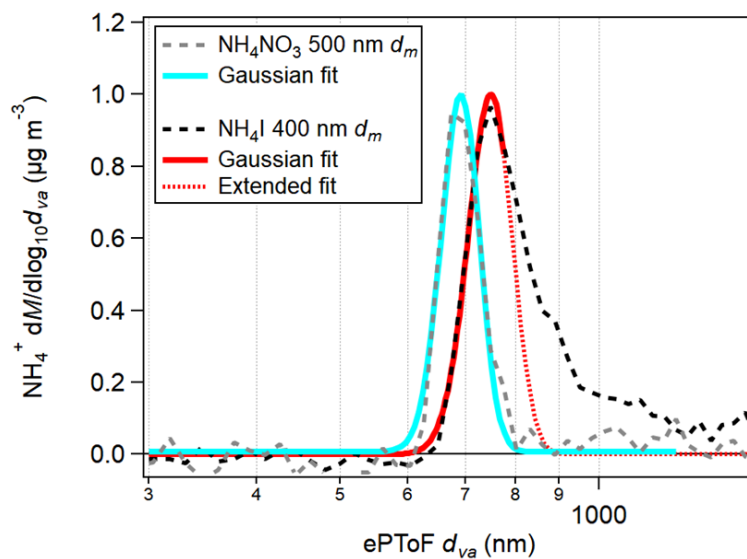
150 **Figure S4.3.** Gaussian fitting of inorganic species for ePToF d_{va} measurements. Volatile inorganic species (NH_4NO_3) were fitted with a full data range. The less/non-volatile inorganic species (NH_4I and $(NH_4)_2SO_4$) were fitted up to a few measurement points beyond the peak (thick red line) so as not to include the broadening on the right shoulder. The right shoulder is an indication of delayed evaporation of less/non-volatile particles on the vaporizer (Drewnick et al., 2015) and thus excluded in the fitting to minimize the potential overestimation of particle size. The measurement of ePToF d_{va} is used to estimate the

155 Jayne shape factor (S) which enters into the conversion of d_{mob} to d_{va} and the calculation of particle mass (Eq. 5 and Eq. 10).

S5. 2D Lens scan stage details and results
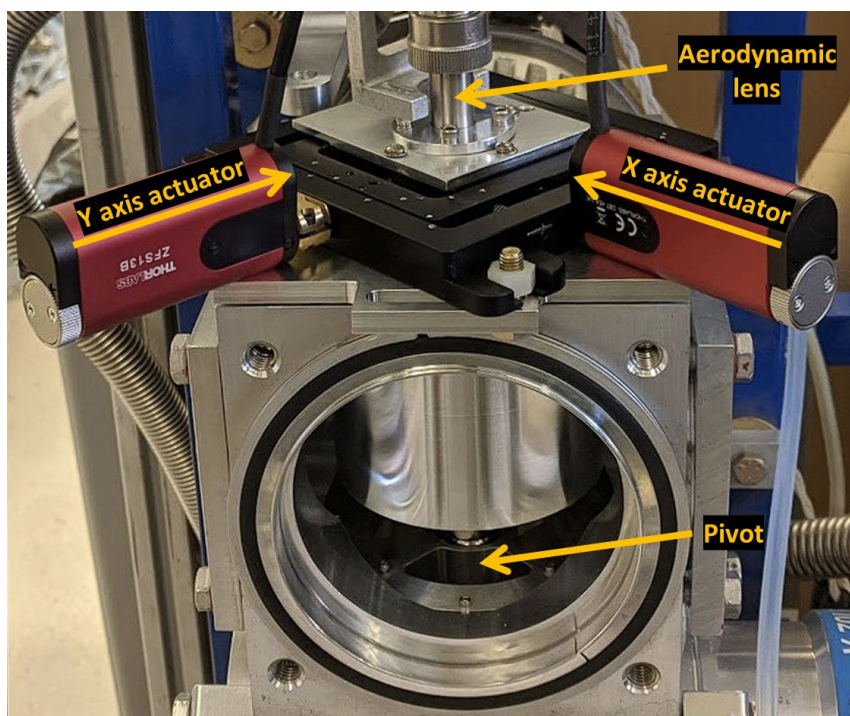
Figure S5.1. Picture of the 2D lens scan stage assembly shown in Fig 3. During operation, the electronic actuator pushes the ADL, changing the aerosol beam direction as its pivot is fixed. During a lens scan, the Y actuator sweeps each leg at 0.05 mm s^{-1}, and then at the end of each Y sweep, the X actuator moves 0.1 mm (Fig. 6). The length from the actuator to the end of ADL is 0.138 m and the length from the end of ADL (pivot) to the vaporizer is 0.348 m. Thus the displacement of the aerosol beam position at the vaporizer plane is equal to -2.65 (negative sign means the actuator direction and beam movement direction are opposite due to the pivot) times the displacement of the actuator.
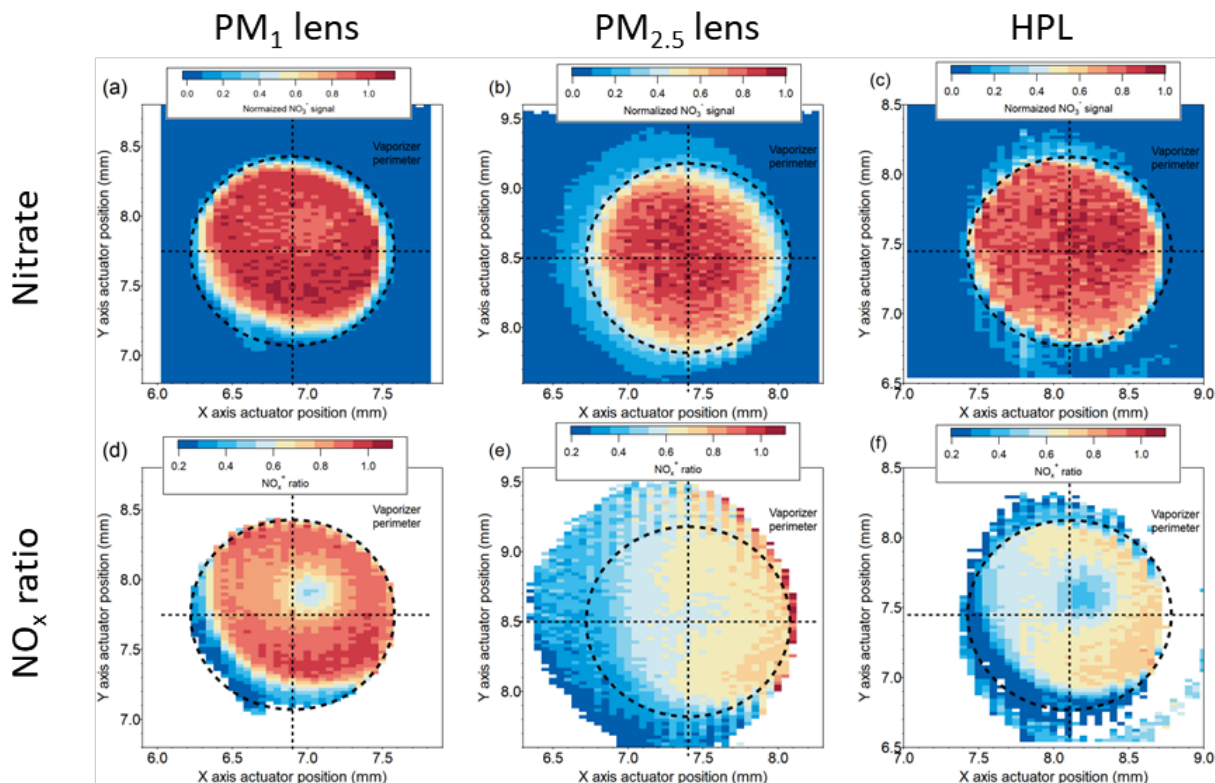
Figure S5.2. Lens scan results from the PM$_1$ lens, PM$_{2.5}$ lens, and HPL (left, middle, right column) in Fig. 7. The top row shows the particle signals normalized by particle concentration, and the bottom row shows the vaporizer position-dependent NO$_x^+$ ratios.
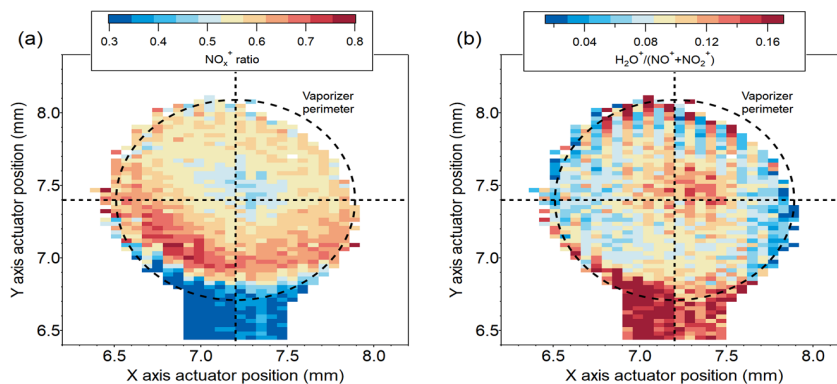
Figure S5.3. (a) NO$_x$ ratio and H$_2$O$^+$/(NO$^+$+NO$_2^+$) from lens scan with a new, not tilted, standard vaporizer used for the TI^{3}GER campaign. These results are from the PM$_{2.5}$ lens and 500 nm d_m NH$_4$NO$_3$ particles. The new standard vaporizer shows a lower NO$_x$ ratio at the vaporizer center. This confirms that the results and conclusions made with lens scans in this work are not specific to the vaporizer used here and, thus, can be applied to standard vaporizers in general.
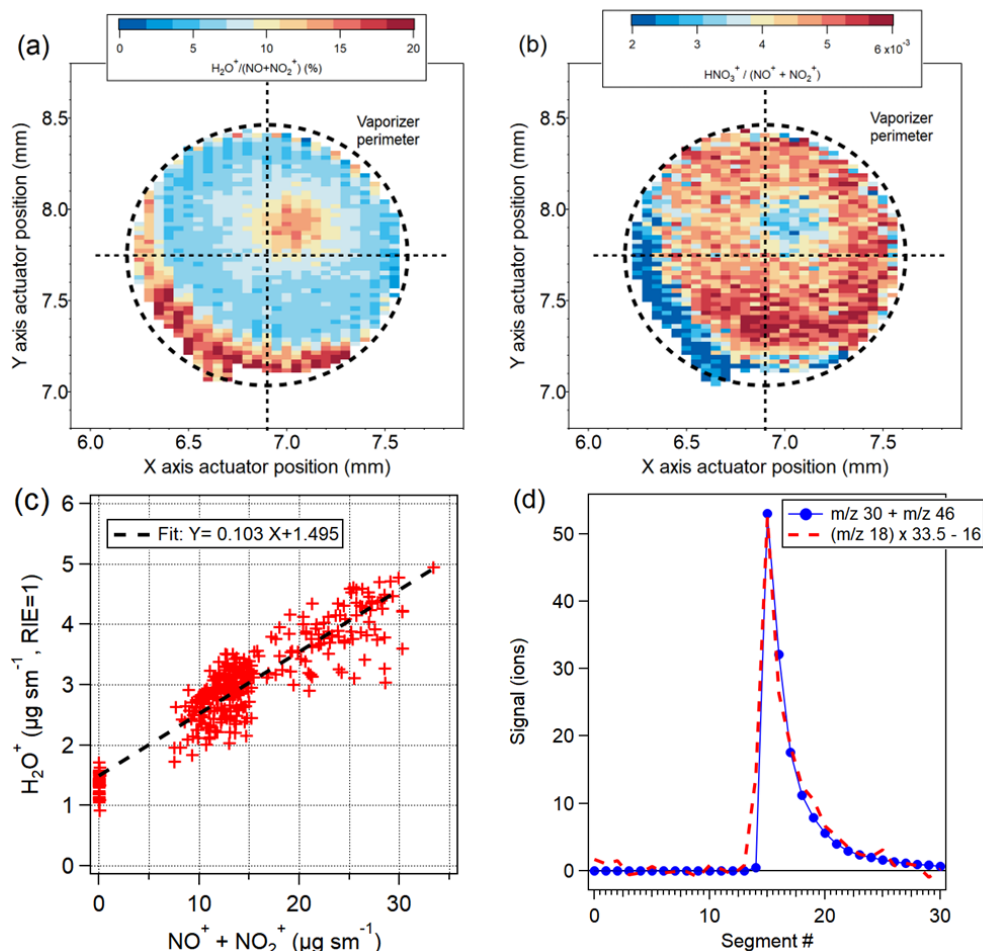
Figure S5.4. Lens scan results are shown for (a) H_2O^+/NO_x^+ and (b) HNO_3^+/NO_x^+. (a) and (b) are results from the same lens scan as Fig. S5.2a. Near the vaporizer center, the H_2O^+ signal was ~ 10% of major nitrate fragments, similar to the MS mode case. At the center of the vaporizer, the fraction increases up to 14-15%. Although noisier than (a), (b) shows a decrease in the HNO_3^+ signal at the center of SV due to higher thermal decomposition of NH_4NO_3. Compared to off-center positions, ~ 25 % of the signal drop was observed. (c) Scatter plot of H_2O^+ and NO_x^+ taken in bulk MS mode using fast mode acquisition. (d) Comparison of nitrate signal (m/z 30 and 46 that correspond to NO^+ and NO_2^+ ions) and water signal (m/z 18 that corresponds to H_2O^+) after background subtraction during event trigger (ET) mode with 500 nm d_m NH_4NO_3 particles. The ion signal is recorded once a single particle is detected. The H_2O+ signal during ET mode was ~ 3 % of major nitrate fragmentation ions. The same aerosol source was used for (c) and (d). ET mode and MS mode were alternated 3 times. In fast mode, the H_2O^+ signal was ~ 10% of major nitrate fragments.
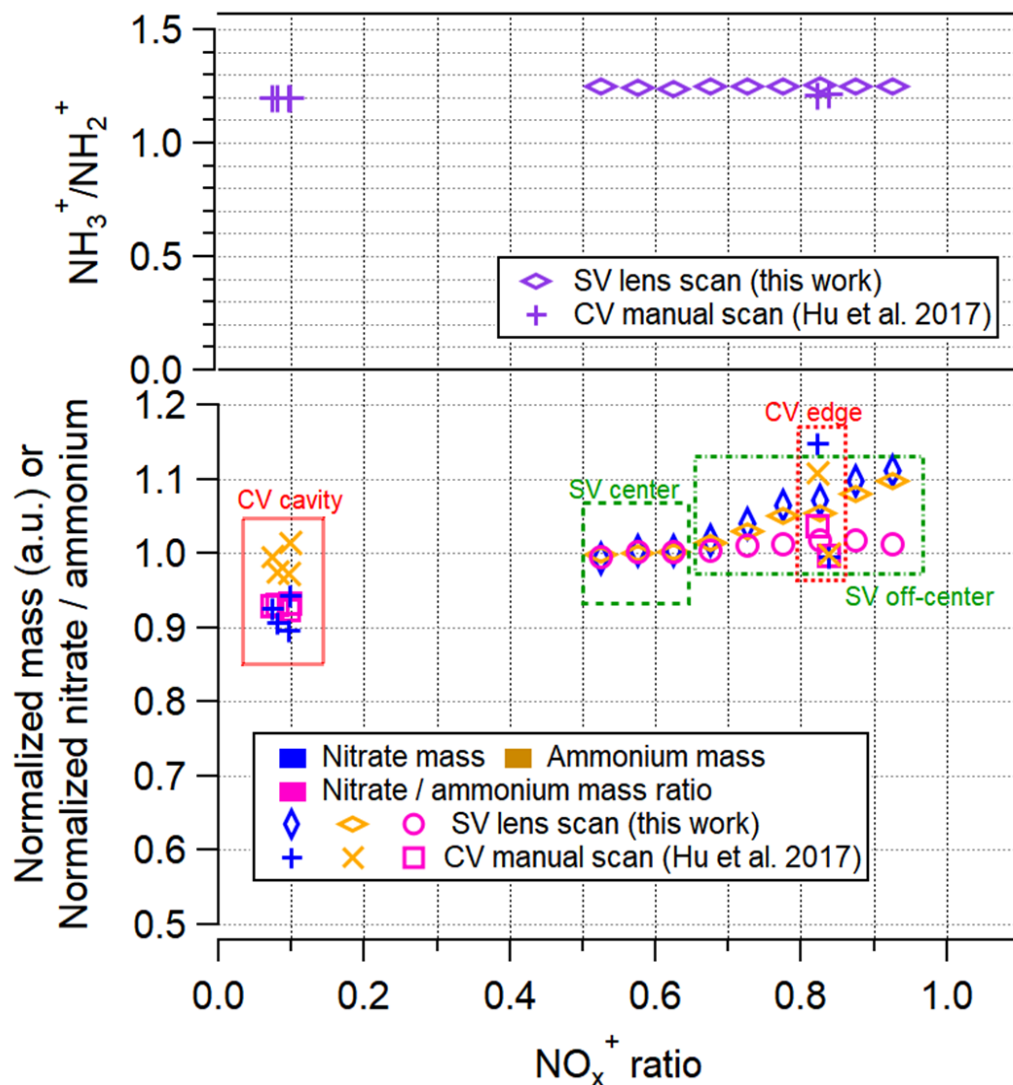
Figure S5.5. (Top) NH_3^+/NH_2^+ and (Bottom) normalized nitrate mass, ammonium mass, and their ratio from NH_4NO_3 particles as a function of NO_x^+ ratio (NO_2^+/NO^+) on a standard vaporizer (SV) and capture vaporizer (CV). In the bottom plot, SV values were normalized by the values at the SV center positions (NO_x^+ ratio ~ 0.5–0.65). Outside of the CV (on the edge of the entrance), the NO_x^+ ratio was comparable to that of off-center positions on SV. CV values were normalized to match the SV values at the CV edge NO_x^+ ratio (0.8–0.85). The CV data was adopted from Hu et al. (2017). Nitrate to ammonium ratio was used to track the nitrate sensitivity due to thermal decomposition (indicated by NO_x^+ ratio). Thermal decomposition if ammonium was constant (as indicated by the NH_3^+/NH_2^+ fragmentation ratio) and thus there is negligible variance in the species of gases ionized after evaporation. However, ammonium mass was ~ 10% lower at the SV center compared to SV off-center positions for unidentified factors, other than thermal decomposition. Therefore, nitrate was normalized by ammonium

in this analysis, to minimize the influence from these unidentified factors. Inside the CV cavity, the NO_x^+ ratio was below 0.1 due to the significant thermal decomposition of $HNO_3(g)$. The nitrate/ammonium ratio was ~ 7–10% lower than the CV edge than SV (assuming that this is not driven by the losses of nitrogen oxides inside the cavity). On the SV center, the ratio was ~ 3% lower than off-center positions. This is probably because the ionized gases consist of less $HNO_3(g)$ and more $NO_2(g)$ and $NO(g)$ in case of more thermal decomposition of nitrate (lower NO_x^+ ratio), such as inside the CV cavity and SV center.

200
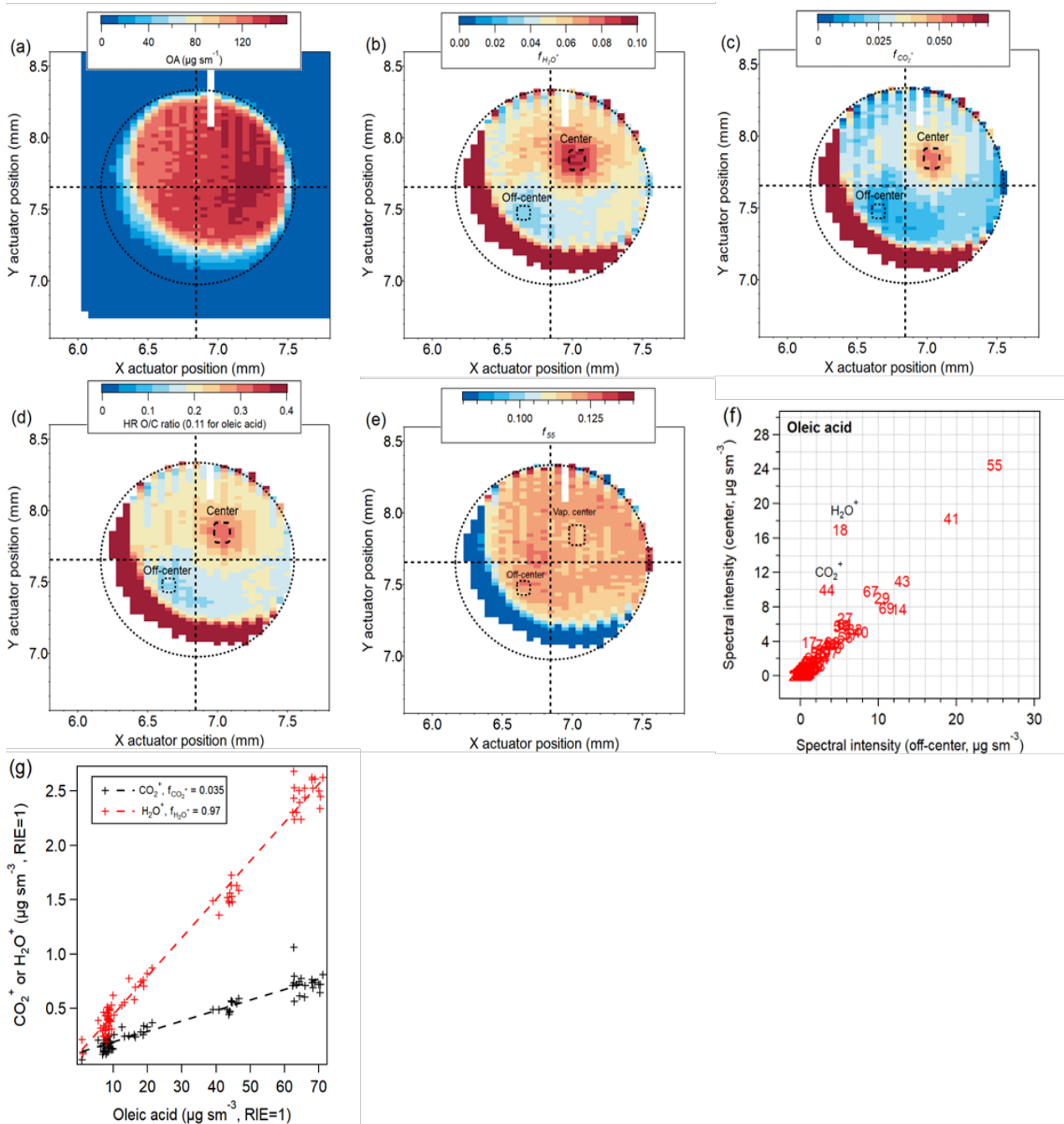
Figure S5.6. Lens scan results of (a) oleic acid mass concentration, (b) f_{H2O+}, (c) f_{CO2+}, (d) O/C atomic ratio, from PM$_1$ lens and 260 nm d_m oleic acid particles, (e) f_{55}. (f) comparison of spectral intensity from oleic acid at the vaporizer center vs. off-center position. The O/C ratio was calculated using the f_{CO2}^+ parametrization from (Canagaratna et al., 2015). Similar to the NH$_4$NO$_3$ case, oleic acid particles produce higher H$_2$O$^+$ and CO$_2^+$ when hitting the vaporizer center, indicating further

210 fragmentations. Higher CO_2^+ results in both higher $f44$ and hence O/C estimation, up to ~ 6 and 2 times higher, respectively, compared to the off-center position. This suggests that the organic CO_2^+ signal may be affected by the particle beam position when measuring ambient organic aerosols, resulting in potentially some instrument to instrument variability in the reported O/C for less oxidized OA as shown in Crenn et al. (2015). Note that during this lens scan, the inlet was pulled by a plumbing line when actuator positions were low. While that resulted in a somewhat distorted lens scan image, it does not affect the

215 results discussed here. (g) linearity between fragment signal (H_2O^+ and CO_2^+) and oleic acid mass at a fixed lens position. The H_2O^+/CO_2^+ ratio from this study that used evaporation-condensation for oleic acid particle generation is ~ 2 and Hu et al. (2018a) that used nebulization with hexane solvent was 2.1.
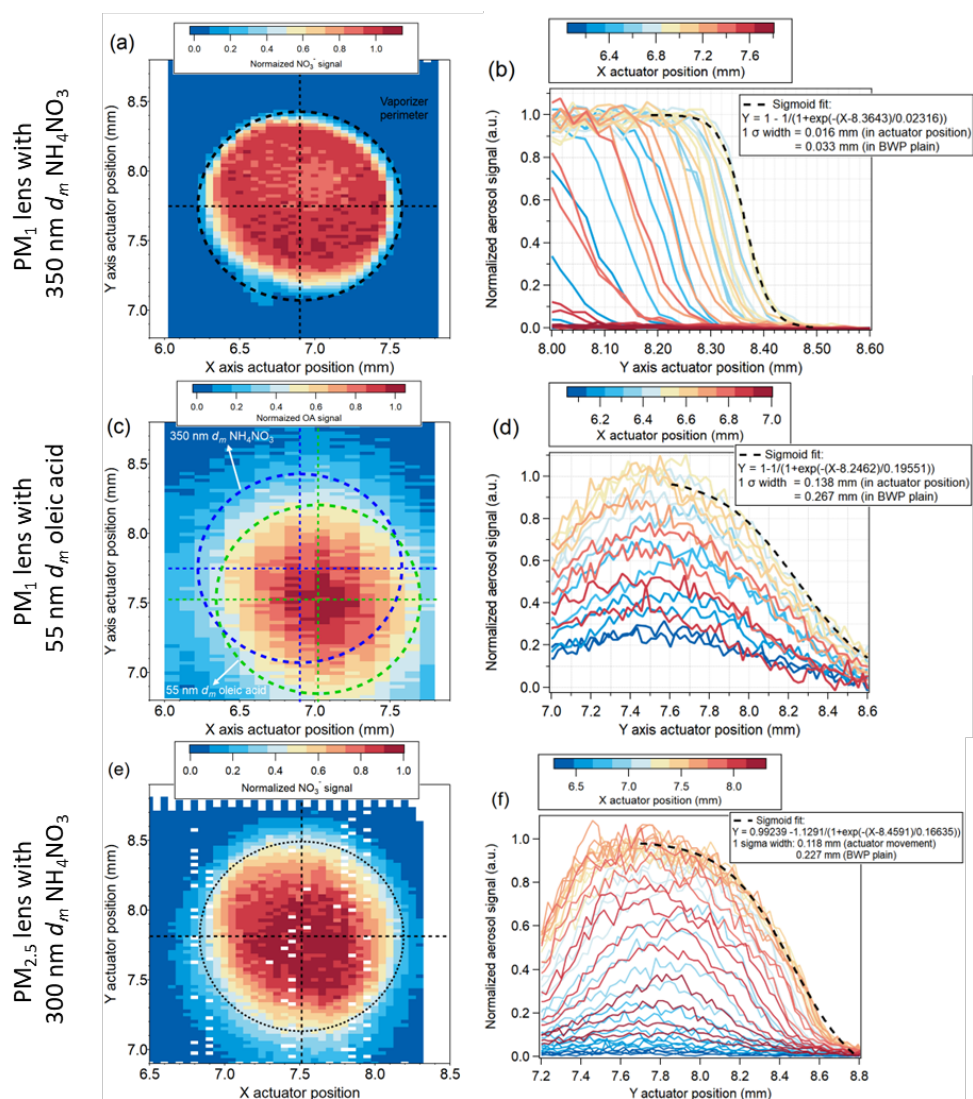
220 **Figure S5.7.** The left column shows lens scan results of the normalized signal of oleic acid or nitrate aerosol. The right column shows the normalized particle signal vs. Y axis actuator position colored by X actuator position during each lens scan. The first row shows lens scan results with the PM$_1$ lens and 350 nm d_m NH$_4$NO$_3$ particles. The second row shows results with the PM$_1$ lens and 55 nm d_m oleic acid particles. The third row shows results with the PM$_{2.5}$ lens and 300 nm d_m NH$_4$NO$_3$ particles. The sigmoidal fit of the Y sweep when the X actuator position corresponds to the vaporizer center shows that the 1 σ beam

225 width of the PM$_1$ lens can be as sharp as 0.033 mm in the BWP plane. The beam width measurement of 55 nm d_m oleic acid with lens scan is not reliable since the beam was too wide that a plateau regime across y actuator position was not obvious. However, the difference in beam center position was identified (Fig. 11b). The beam width of 300 nm d_m NH$_4$NO$_3$ particles was much wider than that from (b) which is consistent with BWP-based beam width measurements (Fig. 11a). More beam width measurements from lens scan are included in Fig. 11a.

230
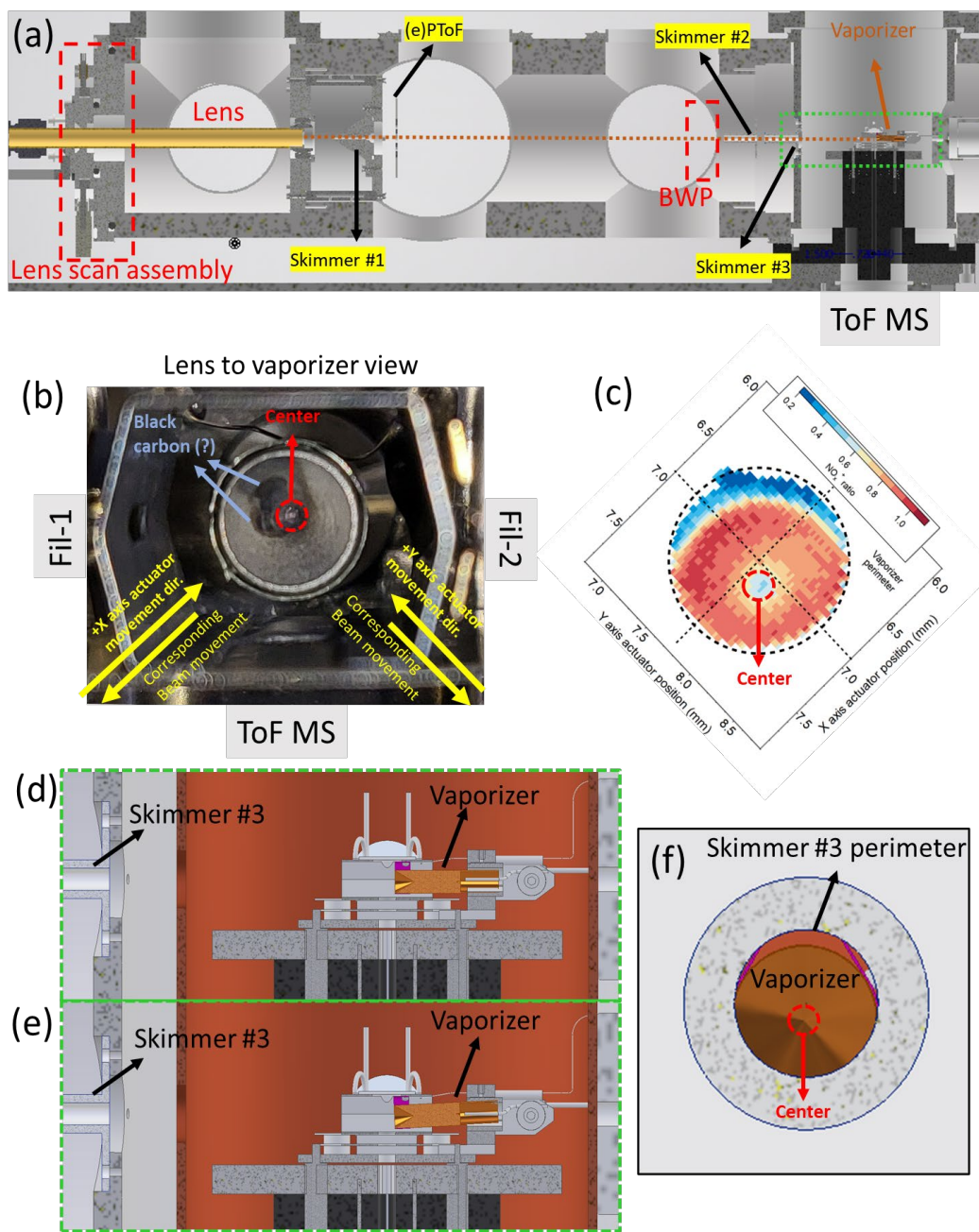
Figure S5.8. (a) Diagram of AMS cross section including the positions of skimmers and vaporizer. (b) Picture of the vaporizer used for all the lab characterizations of the different lenses shown above (which was replaced for the TI^{3}GER campaign). (c) Lens scan with PM$_1$ lens and mapped by NO$_x^+$ ratio. Zoomed in figures of the green dotted box in (a) with different vaporizer misalignment cases: (d) the vaporizer with 0.45 mm higher location and (e) the vaporizer tilted 2.75 degrees downward. (f)
235 Vaporizer blocked by the skimmer #3 as a result of vaporizer misalignments in (d) and (e). The position where the NO$_x^+$ ratio

is low (higher thermal decomposition) is likely the (projected) center of the vaporizer. The fact that the location of the physical center and the center the lens scan do not match indicates that the particle beam is hitting the vaporizer at a certain angle (up to ~3 degrees) and/or height of the vaporizer is misaligned (up to ~ 0.5 mm). The absence of ~60% vaporizer perimeter during lens scan suggests that the ~ 60% of the vaporizer edge was blocked by the third skimmer which implies that the skewed NO_x^+ ratio image from lens scan could be more attributed to the translated vaporizer position.

240

S6. BWP rotation stage and wire position measurement
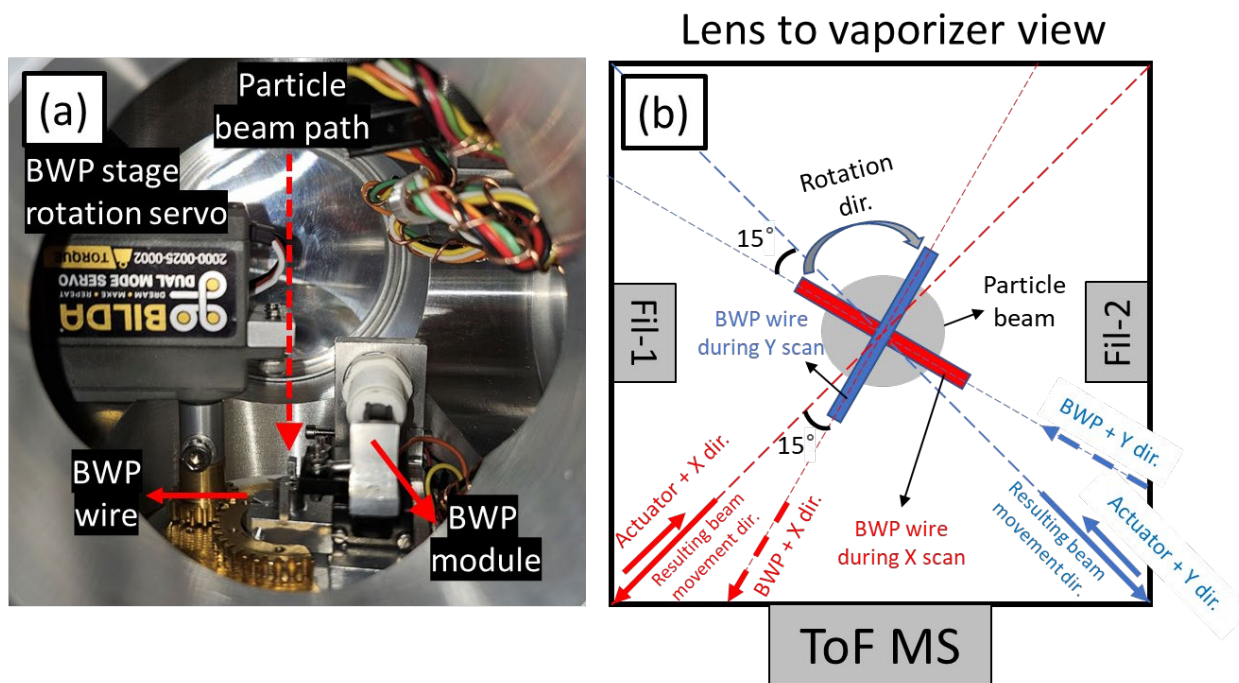
Figure S6.1. (a) Picture of the Aerodyne BWP and the custom-built BWP rotation assembly. (b) Schematic diagram of BWP axes and lens scan actuator axes as aligned for the TI^{3}GER mission (ideally the two coordinate systems are set on top of each other).
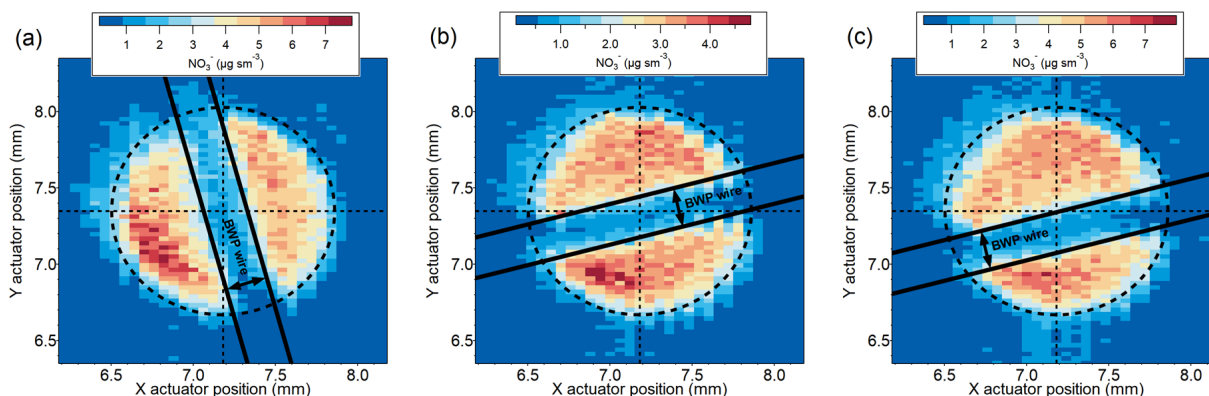
Figure S6.2. Lens scan imaging used to measure the offset of the BWP relative to the vaporizer coordinate system. Ideally, the zero BWP position is located on the line between the lens exit nozzle and the center of the vaporizer. The offset in BWP position can be attributed to many factors including the off-center vaporizer installation and the potential inherent offset in BWP hardware. The lens scan stage was run with the BWP wire parked at a certain position and the BWP was imaged to measure the BWP position relative to the vaporizer center. (a-c) shows the rotation of the beam wire (parked in the center position blocking the middle of the particle beam) while running a sweep with the lens scan, allowing to relate both coordinate systems to each other. Results of lens scans with the BWP wire parked along (a) X axis at +0.5 mm wire position (b) Y axis at +0.6 mm wire position (c) Y axis +0.8 mm wire position. We found that for the TI³GER configuration, the BWP wire set positions along the X and Y axes, +0.5 mm and +0.6 mm, correspond to the vaporizer center position in our setup. As illustrated in Fig. S6.1(b), BWP X and Y axes were 15 degrees off from the lens scan actuator X and Y axes. Notably, the BWP wire position difference between (b) and (c) measured by the lens scan is 0.198 mm which is close to the set wire position difference (0.2 mm). Lens scans were performed with 500 nm d_m NH$_4$NO$_3$ particles with PM$_{2.5}$ lens.

S7. Polydisperse particle generation for 2D-SR-BWP analysis
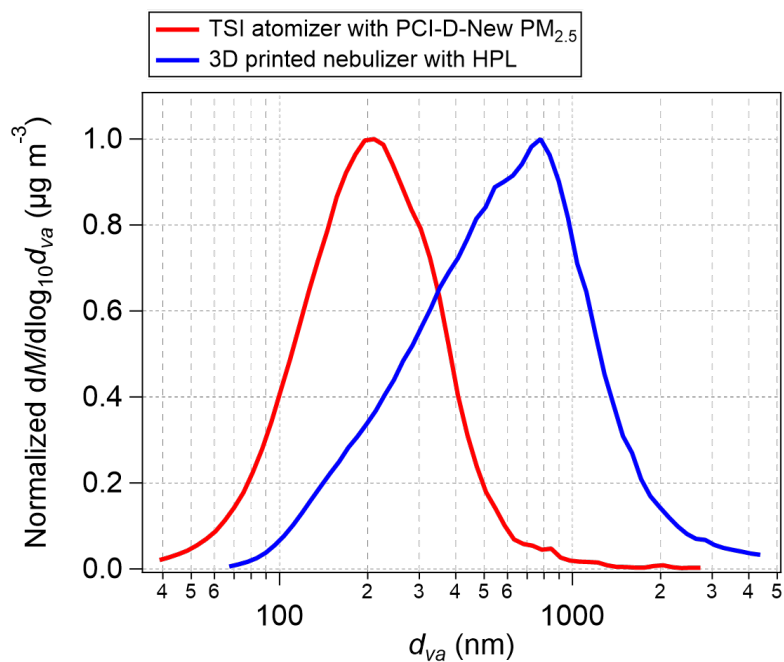
Figure S7.1. Mass size distribution of NH_4NO_3 particles generated by the customized 3D printed nebulizer (blue) and TSI atomizer (model 3076, red). NH_4NO_3 solutions of ~ 0.7 M concentration were used. Most of the measured distributions were within ~ 100% transmission efficiencies of the inlet used for each nebulizer. The nebulizers were operated at ~ 35 psi nozzle pressure.
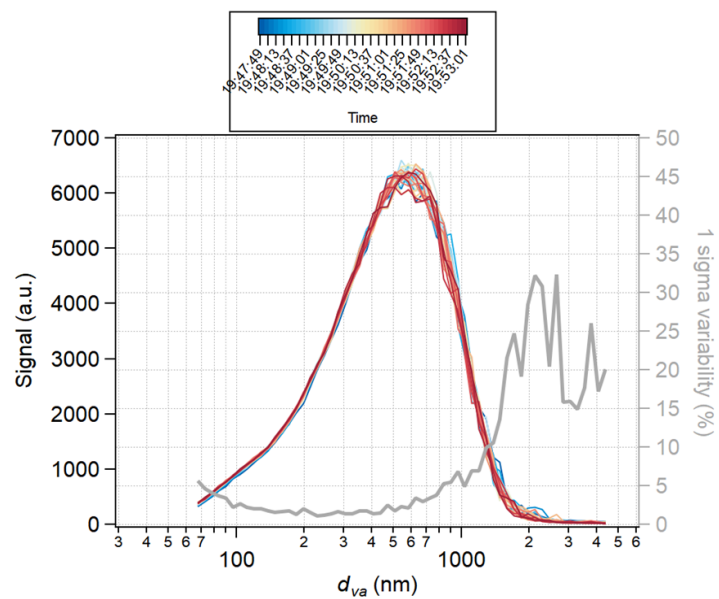
Figure S7.2. Reference size distributions and 1 sigma variability (%) of the regular, unperturbed PToF distributions during the scan along the X axis in Fig. 8.

S8. Particle deposition image
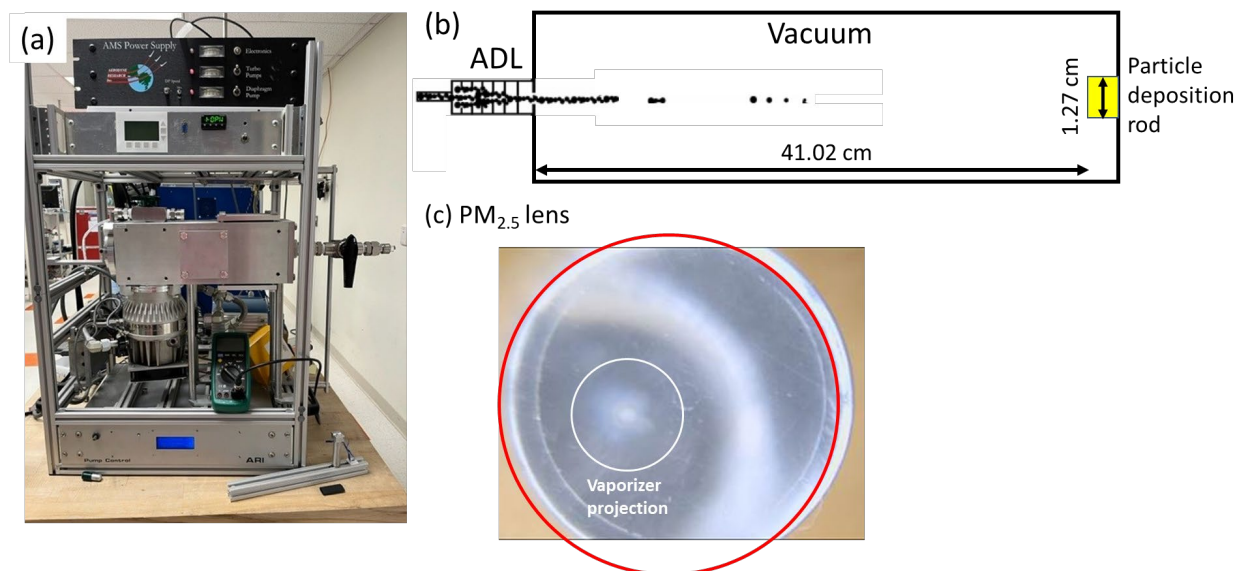
275

Figure S8.1. (a) A picture of the particle deposition system. (b) Schematic diagram of the Aerodyne particle deposition system. (c) The original image of particle deposition tests and the vaporizer perimeter projection (white circles) on the deposition rod were measured with the PM$_{2.5}$ lens beam deposition image. The red solid circles are the perimeter of the particle deposition rod (12.7 mm diameter). Only the particle deposition images within the projected vaporizer perimeters are shown in Fig. 13.

280 The distance between the lens nozzle and rod distance is 0.4102 m. In the CU-HR-AMS system, the nozzle-to-vaporizer distance is 0.3545 m. Assuming radial expansion of the aerosol beam at the end of the nozzle, the projected vaporizer diameter-to-rod diameter ratio is 0.328.

S9. Characterizations of standalone ADLs

Table S9.1. The approximate particle diameter range (E_L = 50%) of the aerodynamic lense transmission efficiency curves is shown in Fig. 14.

Aerodynamic lens type	Reference	$d_{va,50,low}$ (nm)	$d_{va,50,high}$ (nm)	P_{lens} (mbar)	$d_{CO,std}$ (μm)
PM$_1$ lens	Zhang et al. (2004)	45	-	-	-
	Liu et al. (2007)[a]	63	900	-	-
	Liu et al. (2007)[b]	95	650	1.73	100
	Knote et al. (2011)	63	1060	-	-
	This work	47	830	2	120
PM$_{2.5}$ lens	Xu et al. (2017)	150	4000	5.1	-
	Molleker et al. (2020)	< 200	2600	-	100
	This work	55	2700	5.1	120
HPL	Williams et al. (2013)	85	> 3000	18.4	100
	This work	120	> 1500	21	120

[a] at 780 mbar ambient pressure. [b] at 1013 mbar ambient pressure.

Table S9.2. The trapezoid curves in Fig. 14. consist of: – 0 % transmission below $d_{va,0,low}$; – linear increase in transmission vs log(d_{va}), from 0 % at $d_{va,0,low}$ to 100 % at $d_{va,100,low}$; – 100 % transmission from $d_{va,100,low}$ up to $d_{va,100,high}$; – linear decrease in transmission vs log(d_{va}), from 100% at $d_{va,100,low}$ to 0 % at $d_{va,0,high}$.

ADL	$d_{va,0,low}$ (nm)	$d_{va,100,low}$ (nm)	$d_{va,100,high}$ (nm)	$d_{va,0,high}$ (nm)
PM$_1$ lens	34	64	440	1550
PM$_{2.5}$ lens	36	82	1500	5000
HPL	85	170	> 1500	> 1500

Table S9.3. This table shows the ePToF parameters applied to derive Fig 14(d). The v_l values for PM$_{2.5}$ lens and HPL were adopted from Xu et al. (2017) and Williams et al. (2013), respectively. The v_g values were measured by AMS PToF. The D_b and b values were fitted by Eq. 4.

ADL	P_{Lens} (mbar)	v_g (m s^{-1})	v_l (m s^{-1})	D_b (nm)	b (unitless)
PM$_1$ lens	2	746.14	15	4.7305	0.43836
PM$_{2.5}$ lens	5.1	702	15.59	13.045	0.46917
HPL	21	746.1	78.50	30.321	0.73314

Table S9.4. Measured E_L of PM_1, $PM_{2.5}$ lens, and HPL shown in Fig. 14.

PM₁ lens			PM₂.₅ lens			HPL		
d_{va} (nm)	E_L	Compound	d_{va} (nm)	E_L	Compound	d_{va} (nm)	E_L	Compound
31.33	0.024	Oleic acid[a]	35.80	-0.007	Oleic acid[c]	71.60	0.0168	Oleic acid[e]
44.75	0.545	Oleic acid[a]	40.28	0.059	Oleic acid[c]	80.55	0.0436	Oleic acid[e]
49.22	0.742	Oleic acid[a]	44.75	0.126	Oleic acid[c]	98.45	0.1862	Oleic acid[e]
53.70	0.910	Oleic acid[a]	49.22	0.316	Oleic acid[c]	116.35	0.4851	Oleic acid[e]
71.60	1.308	Oleic acid[a]	55.49	0.481	Oleic acid[c]	134.25	0.6646	Oleic acid[e]
107.40	0.853	Oleic acid[a]	62.65	0.688	Oleic acid[c]	161.10	0.8962	Oleic acid[e]
179.00	1.140	Oleic acid[a]	71.60	0.842	Oleic acid[c]	179.00	1.1081	Oleic acid[e]
451.35	1.067	$(NH_4)_2SO_4$[b]	80.55	0.999	Oleic acid[c]	223.75	0.9829	Oleic acid[e]
526.58	0.716	$(NH_4)_2SO_4$[b]	89.50	1.009	Oleic acid[c]	268.50	1.0781	Oleic acid[e]
601.80	0.758	$(NH_4)_2SO_4$[b]	107.40	1.028	Oleic acid[c]	290.88	0.9345	Oleic acid[e]
688.00	0.605	NH_4NO_3	134.25	1.002	Oleic acid[c]	550.40	0.8714	NH_4NO_3
688.00	0.666	NH_4NO_3	179.00	0.934	Oleic acid[c]	602.40	0.8044	NH_4I[f]
752.25	0.667	$(NH_4)_2SO_4$[b]	502.00	0.989	NH_4I[d]	688.00	1.0294	NH_4NO_3
902.70	0.443	$(NH_4)_2SO_4$[b]	688.00	0.980	NH_4I[d]	688.00	1.0511	NH_4NO_3
1053.15	0.304	$(NH_4)_2SO_4$[b]	753.00	0.804	NH_4NO_3	803.20	0.9968	NH_4I[f]
1100.80	0.301	NH_4NO_3	1004.00	0.738	NH_4I[d]	825.60	1.1114	NH_4NO_3
1203.60	0.204	$(NH_4)_2SO_4$[b]	1100.80	0.900	NH_4NO_3	963.20	1.1589	NH_4NO_3
			1255.00	1.000	NH_4I[d]	1004.00	1.0924	NH_4I[f]
			1255.00	0.909	NH_4I[d]	1100.80	0.9889	NH_4NO_3
			1506.00	1.062	NH_4I[d]	1204.80	1.0327	NH_4I[f]
			1757.00	0.991	NH_4I[d]	1405.60	0.8910	NH_4I[f]
			2008.00	0.731	NH_4I[d]	1606.40	0.7943	NH_4I[f]
			2008.00	0.732	NH_4I[d]			
			2259.00	0.651	NH_4I[d]			

[a]RIE = 3.5. [b]S = 0.85, E_b = 0.43. [c]RIE = 3.5. [d]S =1, E_b = 0.55. [e]RIE = 3.04. [f]S = 0.87, E_b = 0.32. S and E_b of NH_4NO_3 are 0.8 and 1 for all the transmission measurements.

300

S10. 2D-SR-BWP results from ADLs
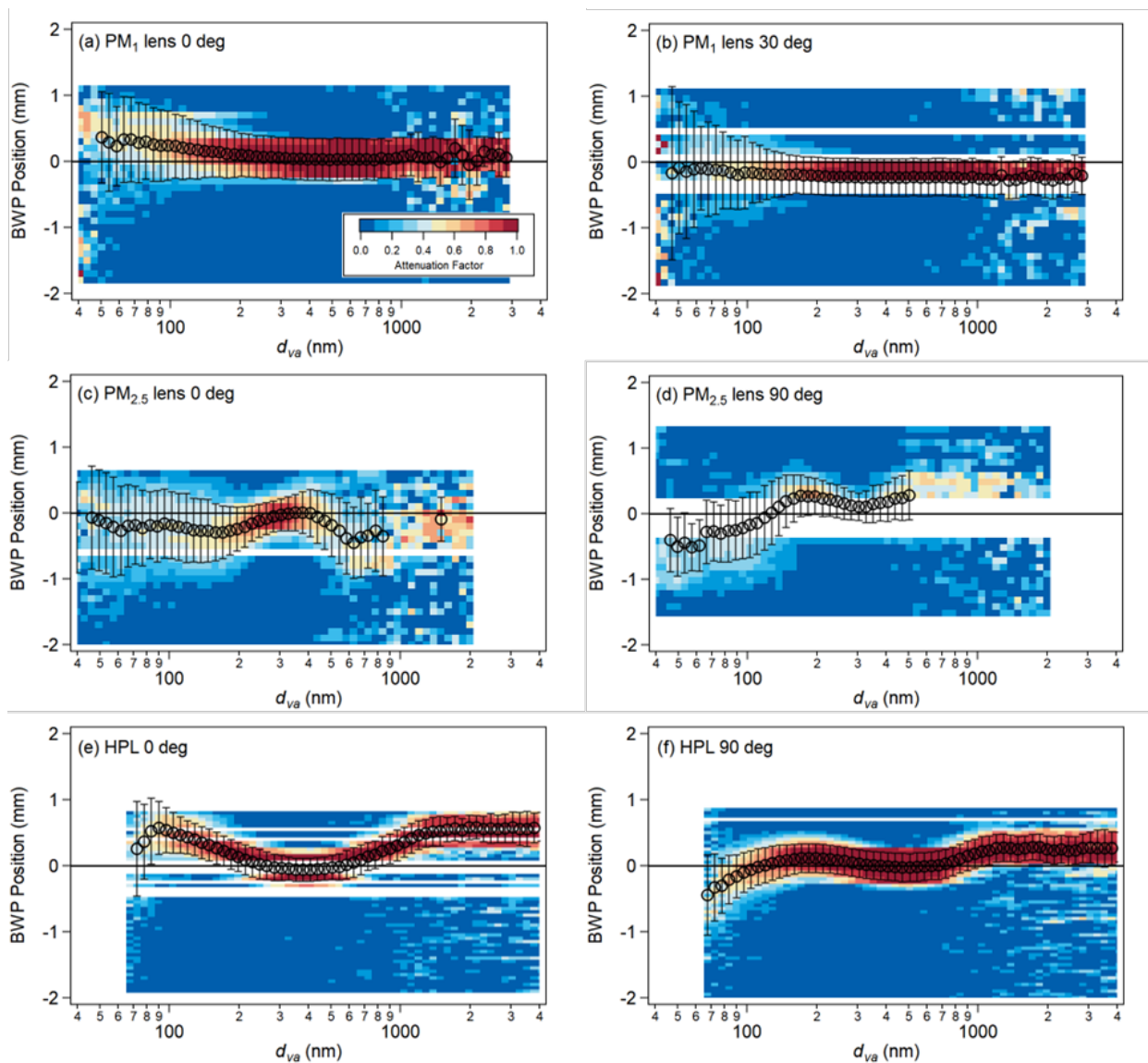
305 **Figure S10.1.** The raw SR-2D-BWP signal attenuations from polydisperse NH_4NO_3 with PM_1 lens (1st row), $PM_{2.5}$ lens (2nd row), and HPL (3rd row) in 0 (left column) and 90 degrees (right column) rotated axis except for (b) which is 30 degree rotation from X axis. Markers and error bars represent fitted center positions and 1 standard deviation from Gaussian fit at each d_{va} size bin. Smoothed signal attenuations by Gaussian fitting are shown in Fig 10.
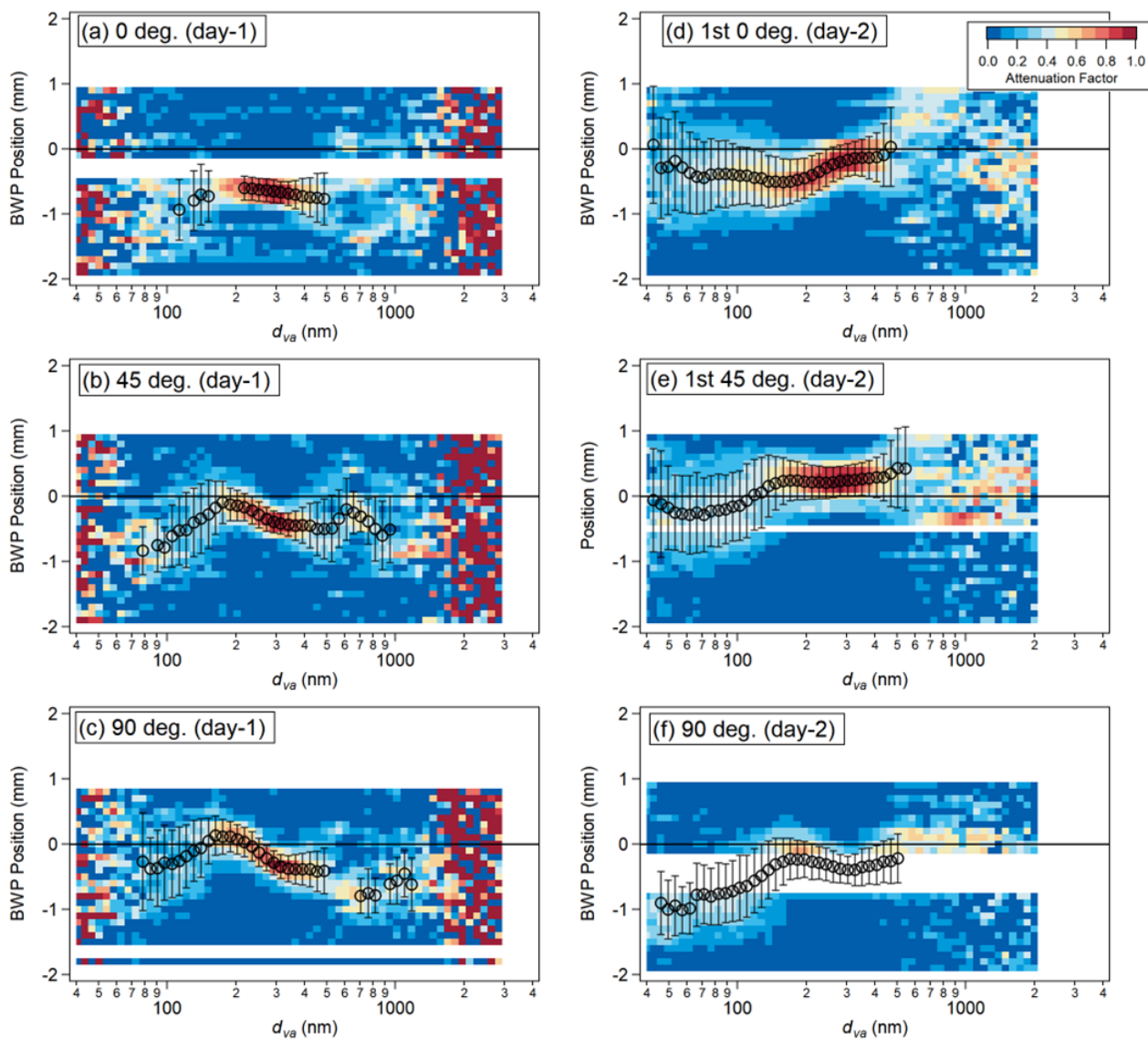
310 **Figure S10.2.** Raw profiles of PM$_{2.5}$ lens in 3 different BWP angles on two different days. The 3D nebulizer performance was compromised for unknown reasons for these experiments and the beam profile signal to noise is low above ~ 800 nm d_{va}. Day-2 profiles were measured after re-installing the lens, hence the orientation of the lens is not the same as Day-1.
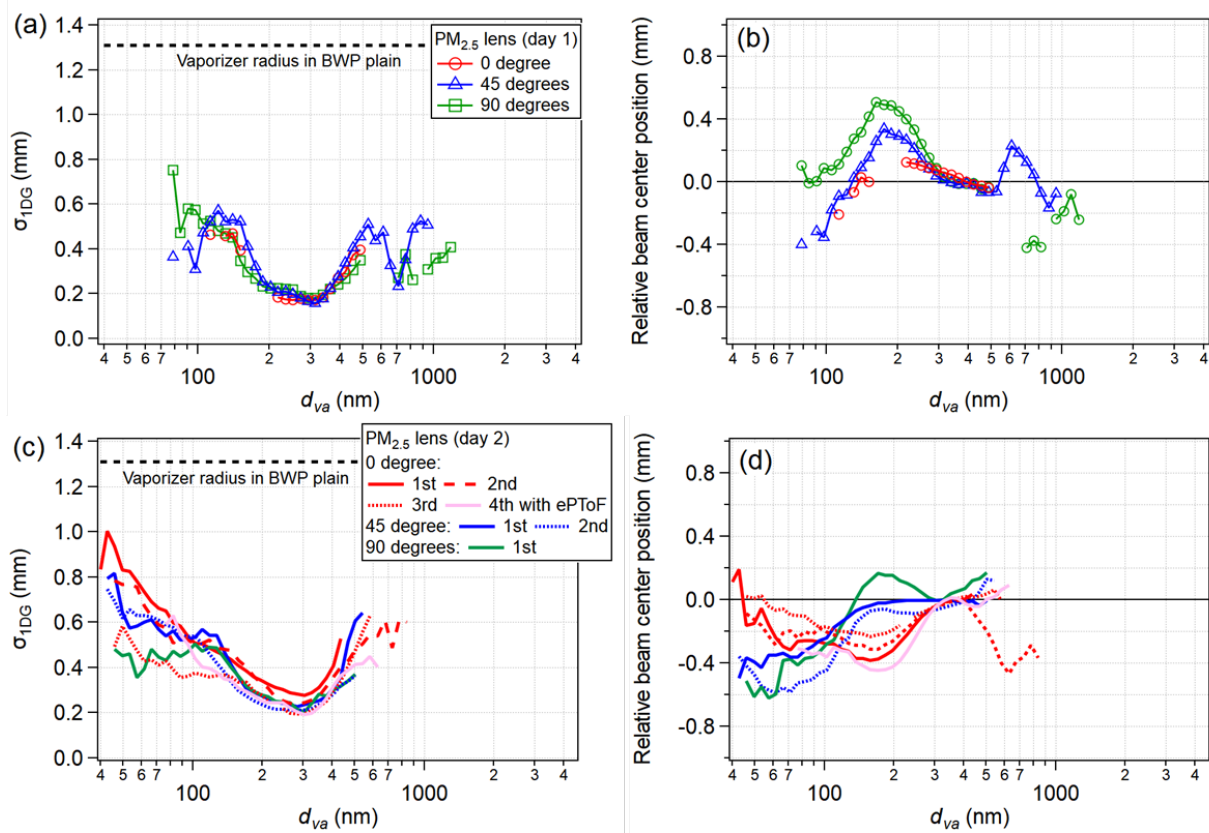
315 **Figure S10.3.** Beam center positions and width as a function of d_{va} shown in Fig. S10.2. Relative center positions are center positions relative to the position at 400 nm d_{va}. The beam width reached a minimum of around 300 nm d_{va}.

S11. PCI comparison
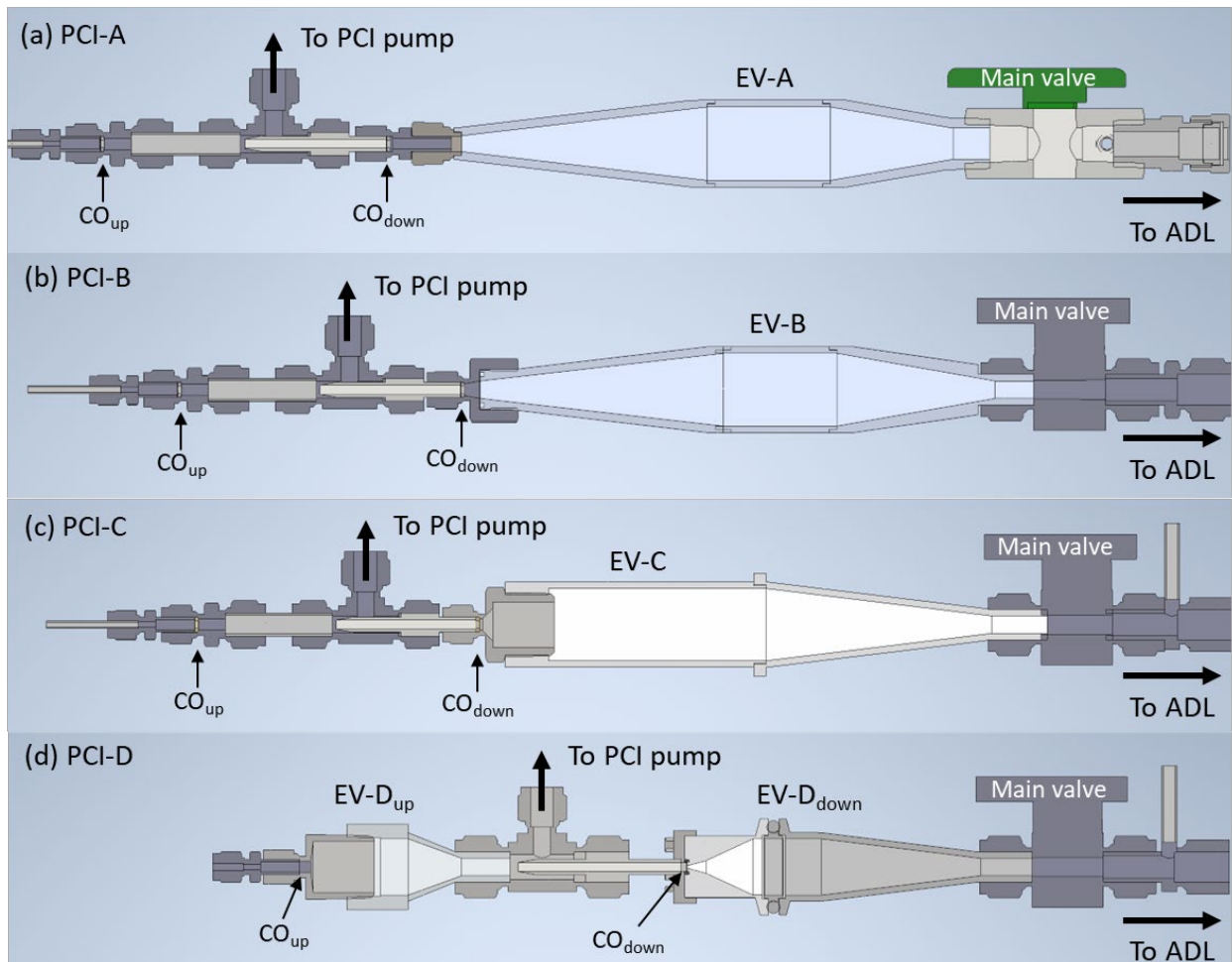
Figure S11.1. Solid models of the four PCIs deployed with CU-HR-AMS during previous field campaigns, following Guo et al., (2021) Fig S7: (a) PCI-A, (b) PCI-B, (c) PCI-C, and (d) PCI-D. All PCIs consist of a PCI pump port between two critical orifices (CO_{up} and CO_{down}) as well as a custom-designed expansion volume downstream of CO_{down} to minimize particle losses. Details on expansion volume designs for PCI-A, PCI-B, and PCI-C are discussed in Guo et al. (2021). Another expansion volume was added to PCI-D downstream of CO_{up} since it significantly reduced particle losses. More operational details on the four PCIs can be found in Table S11.1.

Table S11.1. Comparison of setup and performance of PCIs (and ADLs) utilized for CU-HR-AMS airborne measurements in various field campaigns. The optimal altitude range is the altitude range range where P_{PCI} can be kept constant during flight
330 (assuming ambient T = 0°C). During the ATom-1 campaign, both PCI-B (for the earlier part) and PCI-C (for the later part) were used.

PCI name used in this work	PCI-Bahreini	PCI-A	PCI-B	PCI-C	PCI-D	
Reference	a, b, c	d	d,e,f	d	This work	
Field campaigns deployed	MILAGRO, INTEX-B	ARCTAS, DC3	SEAC⁴RS, WINTER, KORUS-AQ ATom-1 (first half)	ATom-1 (second half) ATom 2-4, FIREX-AQ	TI³GER	
ADL type	PM$_1$				PM$_{2.5}$	
P$_{lens}$ (mbar)	1.9–2.1				5.1	
d_{CO1}/d_{CO2} (µm)	180/150	300/250	300/250 (SEAC⁴RS, ATom-1) 300/170 (WINTER, KORUS-AQ)	350/220	450/350	450/300
Set P_{PCI} (mbar)	466.7	122	122 (SEAC⁴RS, ATom-1), 425 (WINTER, KORUS-AQ)	250	96	122.6
Optimal altitude range (km)	0 - 5.7	0-13	0-13, 0-8	0 - 10	1.7 - 16	0 - 14.6
$d_{va,50,low}$ (nm)	N/A*	N/A*	N/A*	50	60	60
$d_{va,50,high}$ (nm)	> 500	N/A	500-600, 850	750 (ATom 1-2) 770 (ATom 3) 920 (Atom 4) 960 (FIREX-AQ)	1400	1300

a: Bahreini et al. (2008), b: DeCarlo et al. (2008), c: Dunlea et al. (2009), d: Guo et al. (2021), e: Schroder et al. (2018), f: Nault et al. (2018), *Although $d_{va,50,low}$ values were not measured, these are expected to be similar to $d_{va,50,low}$ of PM$_1$ lens (~ 50 nm).

335   **Table S11.2.** The trapezoid curves in Fig. 15 consist of: – 0 % transmission below $d_{va,0,low}$; – linear increase in transmission vs $\log(d_{va})$, from 0 % at $d_{va,0,low}$ to 100 % at $d_{va,100,low}$; – 100 % transmission from $d_{va,100,low}$ up to $d_{va,100,high}$; – linear decrease in transmission vs $\log(d_{va})$, from 100% at $d_{va,100,low}$ to 0 % at $d_{va,0,high}$.

PCI-ADL	d_{CO1}/d_{CO2} (µm)	$d_{va,0,low}$ (nm)	$d_{va,100,low}$ (nm)	$d_{va,100,high}$ (nm)	$d_{va,0,high}$ (nm)
PCI-C-PM$_1$	350/220	33	78	550	1700
	350/300	-	-	300	1500
	350/350	-	-	230	1500
	500/400*	30	65	150	3500
PCI-C-PM$_{2.5}$	350/220	-	-	750	2500
	350/300	-	-	400	2500
	350/350	40	80	250	2300
	500/400*	50	80	200	6000
PCI-D-PM$_{2.5}$	350/300	-	-	830	2000
	350/350	40	75	830	2300
	500/400	-	-	700	1700
PCI-D-HPL†	500/400	110	170	1000	3300

*Does not follow a trapezoid curve, see Fig. 15. †See Fig. S11.2.

340
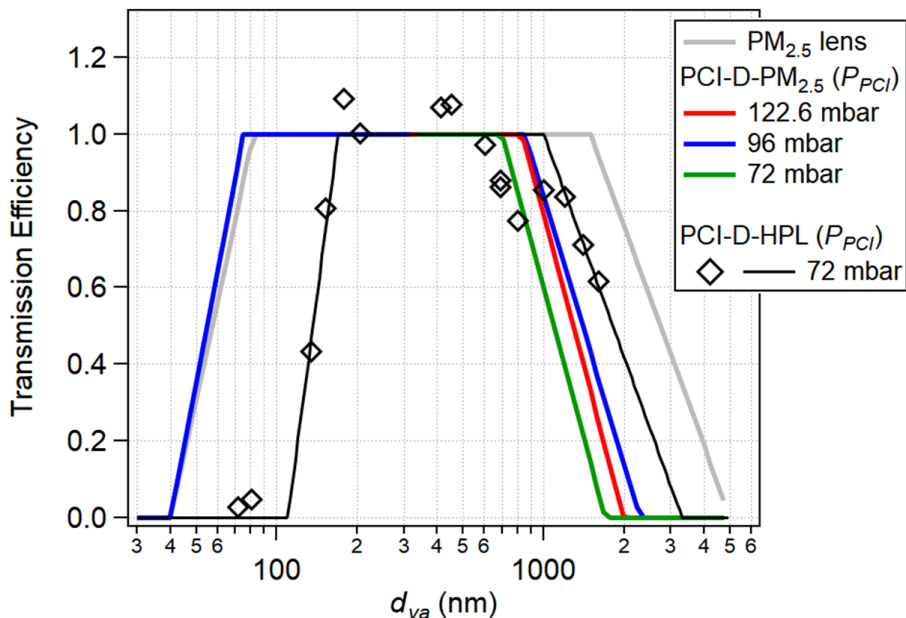
Figure S11.2. Transmission efficiency of PCI-D-HPL (P_{PCI} = 72 mbar) in comparison to PCI-D-PM$_{2.5}$ at different P_{PCI}.
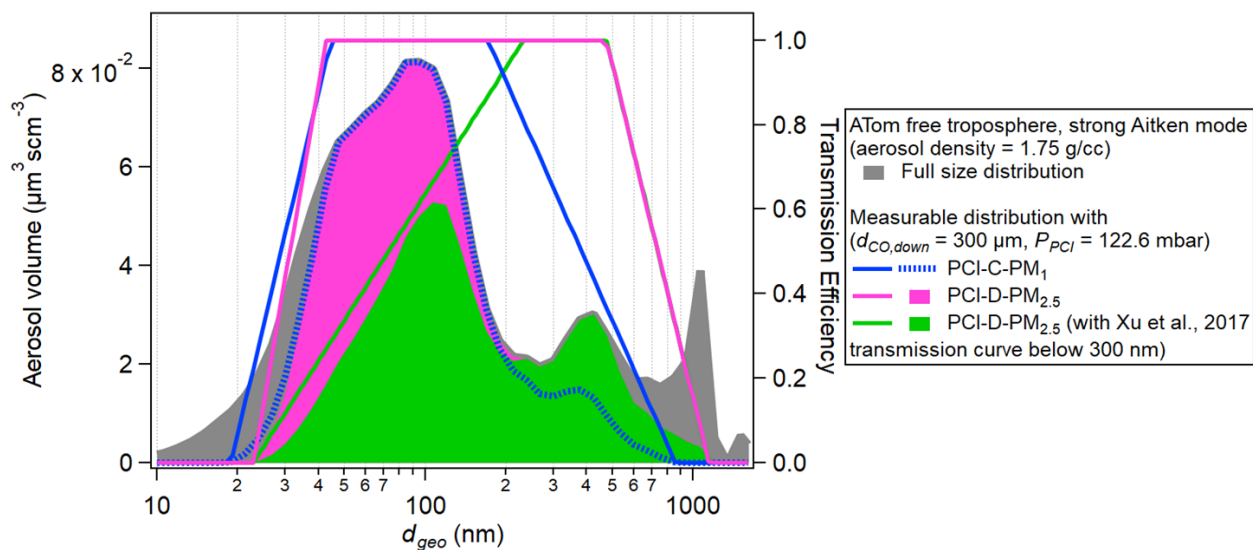
345   **Figure S11.3.** Measurable size distribution with three different inlet configurations in the upper troposphere when there was strong Aitken mode aerosols during ATom campaign. Compared to the inlet with PM$_1$ lens, sampling efficiency of Aitken mode aerosols wih PCI-D-PM$_{2.5}$ inlet was not significantly compromised. If the transmission efficiency measured by Xu et al. (2017) is applied (below 300 nm) to the inlet, Aitcken mode sampling efficiency is significantly compromised.
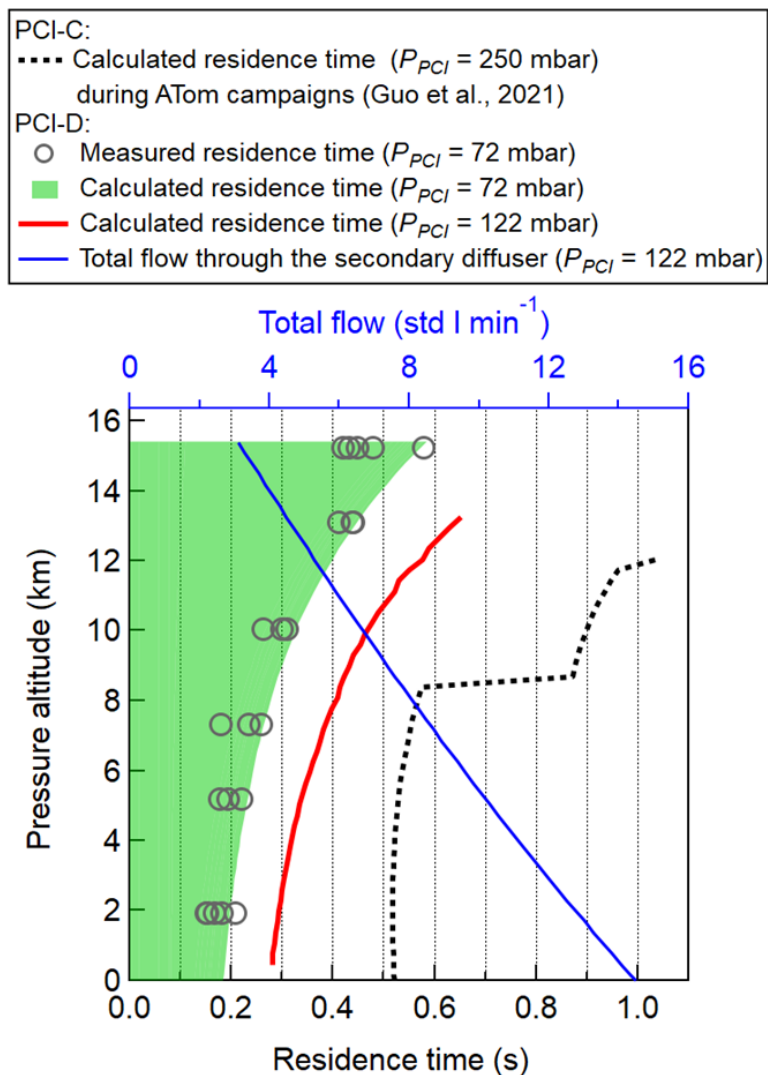
Figure S12.1. The residence time (RT) of the PCI design in Bahreini (2008) is long (~ 5s) due to a large internal volume. For the PCI-C, the residence time has been improved by reducing both the length and ID and using an improved internal takeoff design, to achieve an internal volume of only 3.5 cm³ (vs. ~30 cm³ in Bahreini et al., 2008) (Guo et al., 2021). In this work, 355   the residence time (from the entrance of PCI ,i.e., CO_{up}, to the AMS vaporizer) of PCI-D has been calculated using simple linear plug flow assumptions and experimentally measured using calibration particle puffs (Fig S12.2). RT of PCI-D is 0.2-0.5s depending on the altitude (inlet pressure) which is ~ half of PCI-C. The shortened residence time was achieved mostly due to the reduced expansion volume and lower PCI pressure.
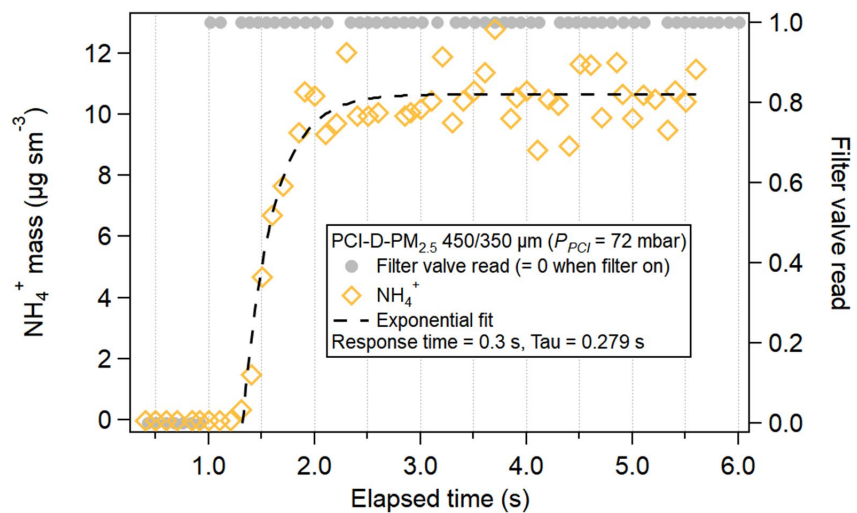
360 **Figure S12.2.** An example of residence time measurement with NH_4NO_3 shown in Fig. S12.1. Both filter valve status and AMS data are acquired at 10 Hz. The tau from exponential fit is the characteristic residence time of aerosol downstream of CO_{up}.

S13. Effect of P_{Lens} on small particle transmission
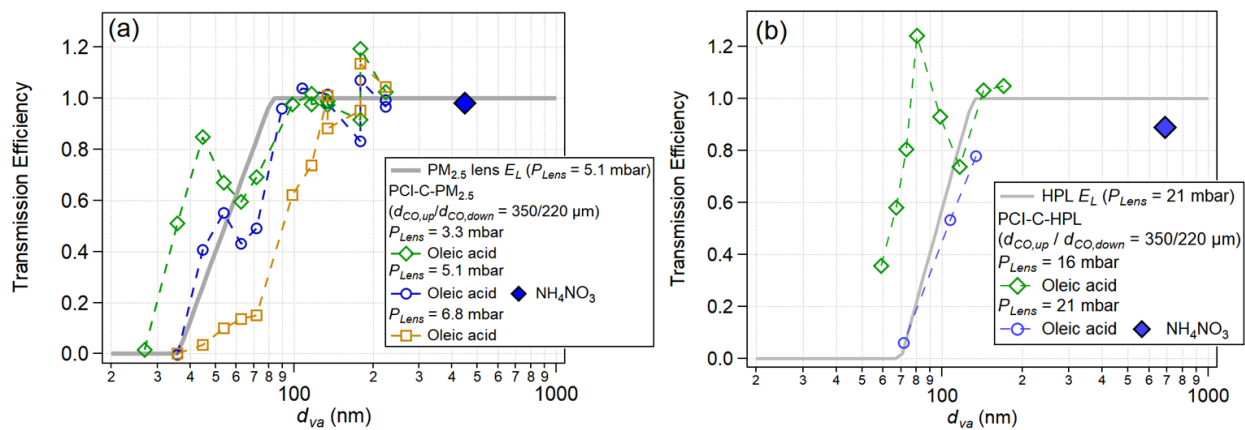
365

Figure S13.1. Particle transmission of PM$_{2.5}$ lens and HPL was measured at different lens pressures. PCI-C was used to reduce lens pressure.

370 **S14. TI³GER campaign details**

Table S14.1. Location and critical orifice configuration for each flight during TI³GER. RF: Research Flight, FF: Ferry Flight between CO and HI.

Flight number	Date	Location	d_{CO1}/d_{CO2} (μm)
RF01	04/02/2022	CO	450/350
RF02	04/07/2022	CO	450/350
FF01	04/11/2022	CO to HI	450/350
RF03	04/13/2022	HI	450/350
RF04	04/15/2022	HI	450/350
RF05	04/20/2022	HI to AK	450/300
RF06	04/21/2022	AK to HI	450/300
RF07	04/23/2022	HI	450/300
RF08	04/27/2022	HI	450/300
FF02	04/29/2022	HI to CO	450/300
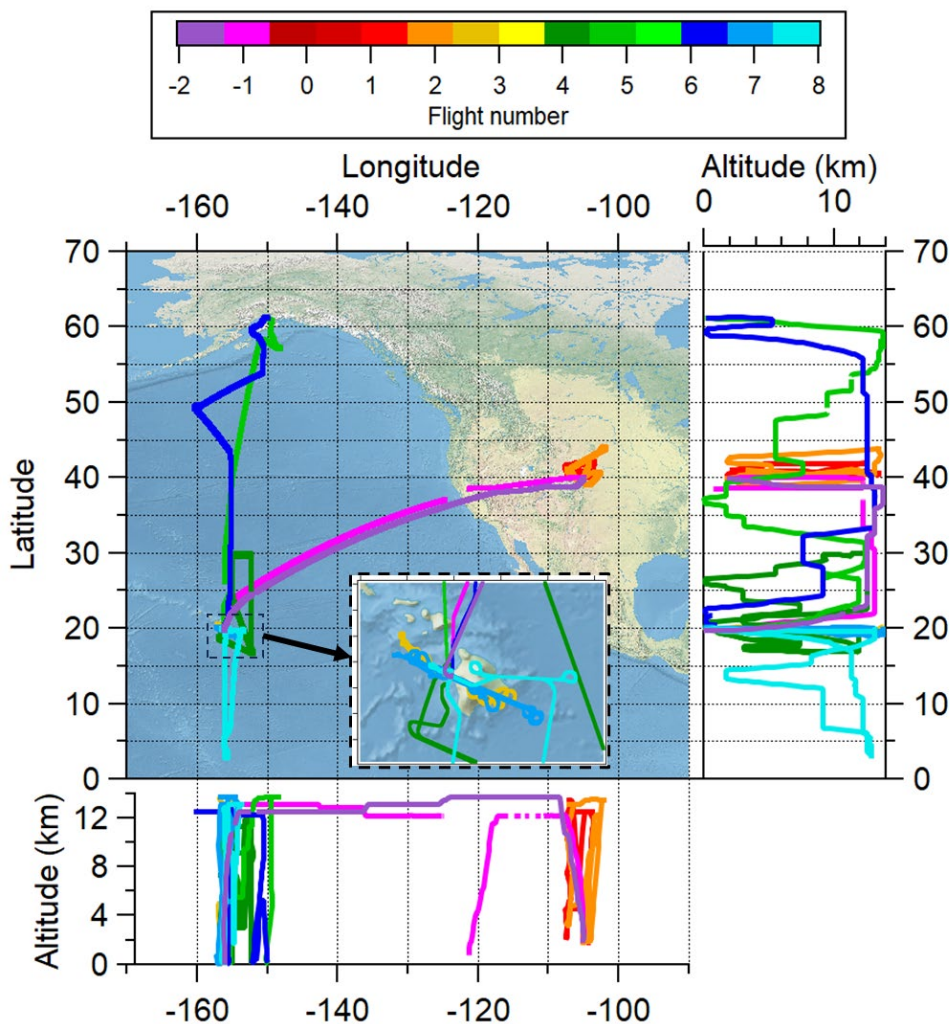
375

Figure S14.1. Flight track and altitude during the TI³GER campaign. The positive flight numbers are research flight numbers. The negative numbers stand for the ferry flights from CO to HI (FF01, "-1") and HI to CO (FF02, "-2"), respectively. Note that data were gathered during the ferry flights and were included in the analysis of this study.

380

S15. AMS calibration during TI³GER
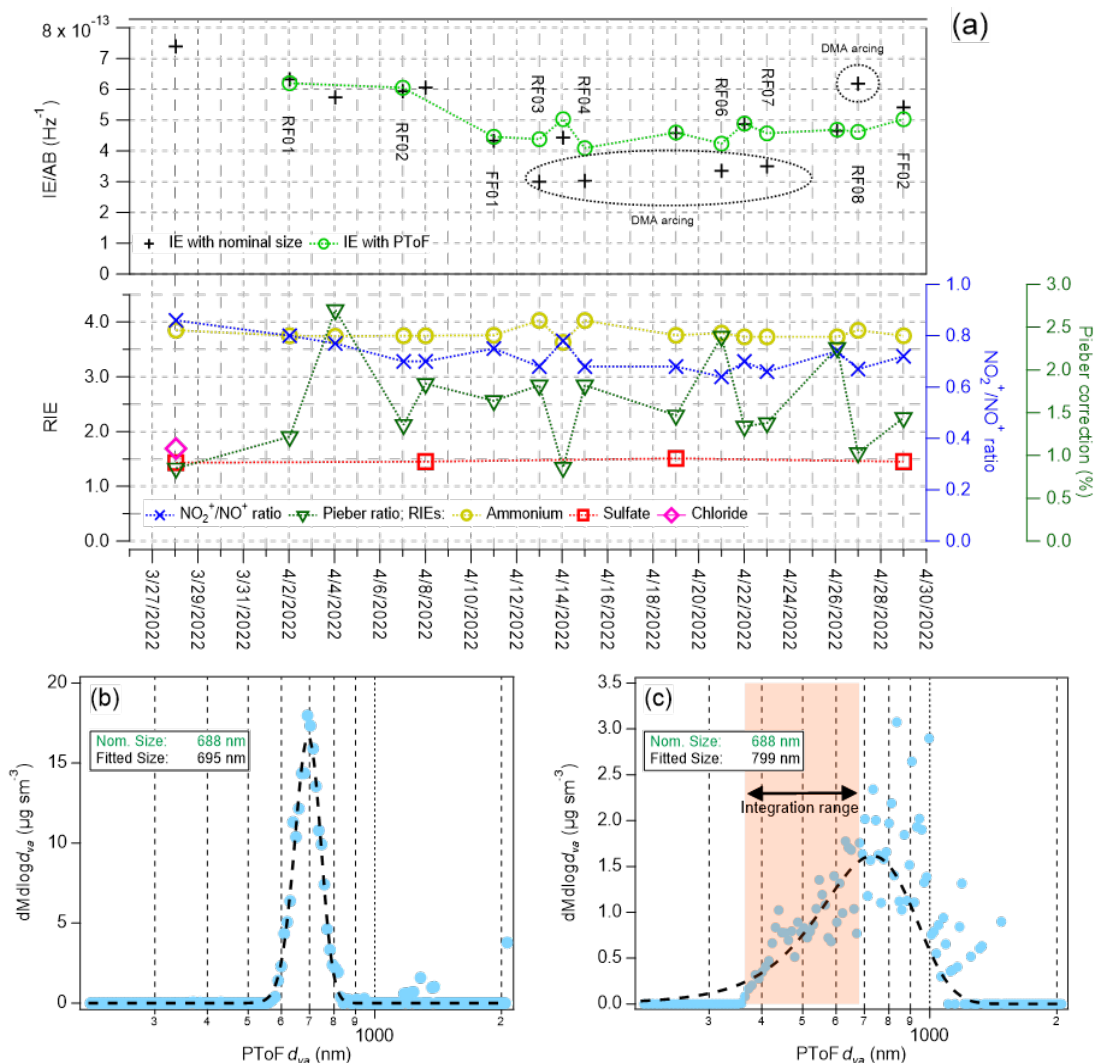
Figure S15.1. (a) Ionization efficiency (IE) and relative ionization efficiency (RIE) of major species during the TI³GER
campaign. The Pieber correction is the amount of CO_2^+ signal generated by nitrate reaction on the vaporizer (Pieber et al.,
2016). For the event trigger (ET) calibrations after flights, the DMA was placed outside the airplane and the particles were
delivered to the AMS inside the airplane. In HI (after RF03-RF08), the DMA output was not very stable showing signs of
arcing as shown in (c), potentially due to nitrate evaporation in the hot DMA. When the output of DMA was not monodisperse,
IE was estimated based on the particle sizes measured by PToF during ET cycles (green circles). The particle size range where
the distribution is reasonable without too much noise was selected. Particles outside of the size range were excluded from the
IE analysis. When the DMA output was monodisperse, as shown in (b), the mobility diameter was used to calculate the volume
of calibration aerosol (black cross in (a)). In those cases, both methods yield comparable IE.

S16. BWP results during the TI³GER campaign
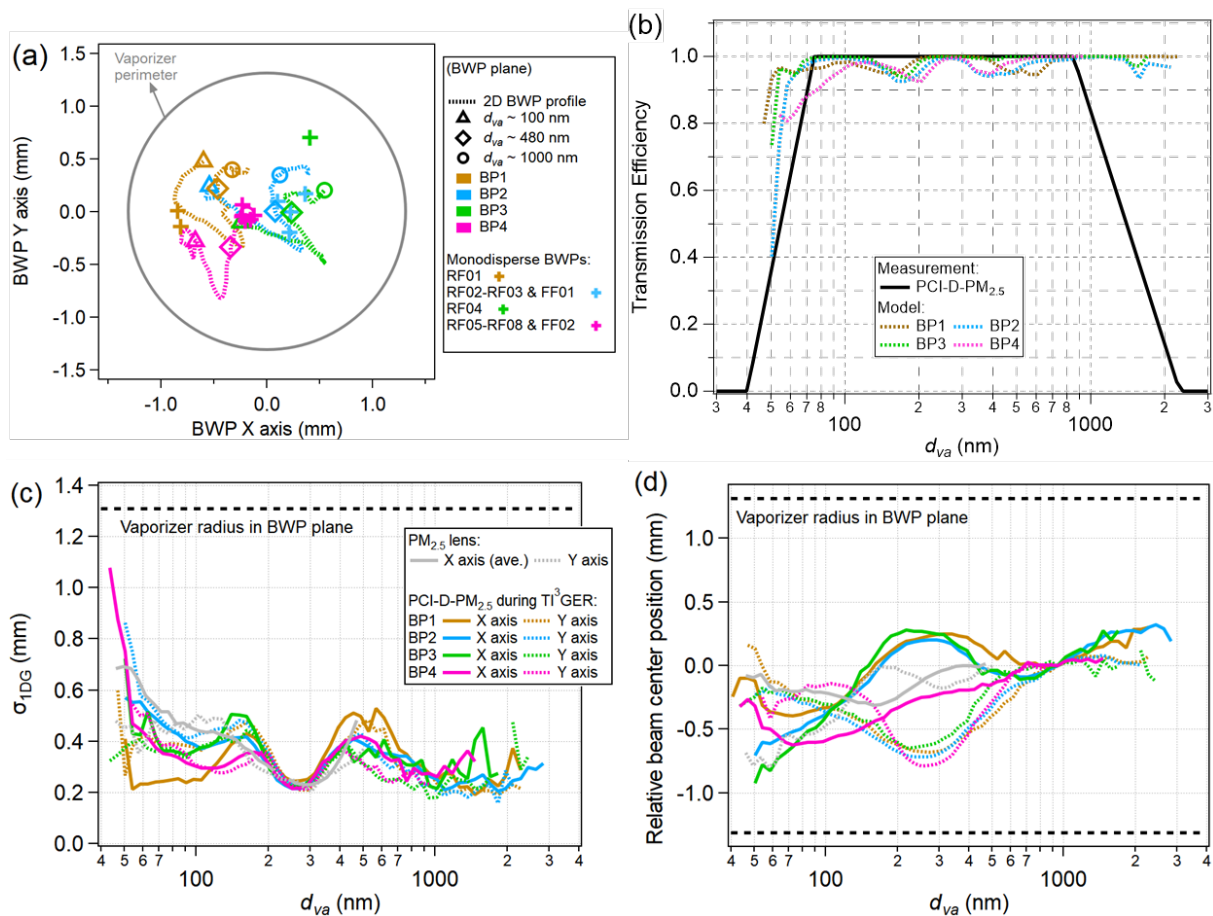
Figure S16.1. (a) Compilation of beam center positions as a function of d_{va} measured from 2D-SR-BWP analysis during TI³GER campaign (dashed lines). The gray circle is the vaporizer perimeter at the BWP plane. The triangle, diamond and circle markers represent beam center positions of ~100, ~480, and ~1000 nm d_{va}, respectively, from each beam profile from 2D-SR-BWP (BP1-BP4). Cross markers are beam positions of 2D-BWP with monodisperse aerosols after flights. After performing each 2D-SR-BWP, the inlet system was secured with screws which can move the lens during the process. In order to obtain the beam profiles after securing the lens, the profiles were moved to match with the monodisperse 2D-BWP after flights (Fig. 16). These four 2D-SR-BWP measurements were performed on 4/4 (between RF01 and RF02), 4/5 (between RF01 and RF02), 4/14 (between RF03 and RF04), and 4/16/2022 (between RF04 and RF05), respectively. After BP1, PCI was cleaned and re-installed. BP2 was measured after lens adjustment toward the center. BP3 was measured just for check without changes in the inlet. However, the lens seemed to be moved during inlet lockdown after BP3 or during RF04 for some reason. BP4 was measured after switching CO_{down} from 350 μm to 300 μm. Also, CO_{up} was cleaned after BP4. (b) Modeled particle transmission (markers) from the four 2D-SR-BWPs and the measured TE (solid line) of PCI-D-PM₂.₅ with 450/350

μm ($d_{CO,up}$ / $d_{CO,down}$). These TEs are before correcting the profiles to match with monodisperse 2D-BWPs. (c) σ_{IDG} and (d) relative beam center position of BP1-BP4 and the PM$_{2.5}$ lens in the X and Y axes as a function of d_{va}. The results from the PM$_{2.5}$ lens are from Fig. S10.3c-d. There were several reconfigurations of the AMS inlet since the experiments in Fig. S10.3c-d, thus the rotational orientation of the PM$_{2.5}$ lens in those experiments was different from the TI³GER configuration, and thus, X and Y axes do not necessarily represent the same axial beam information between the two cases. Regardless, (c) shows that beam width in two different axes are similar (i.e., beam cross section is circular) and the addition of PCI-D does not significantly change the beam width. In (d), the PM$_{2.5}$ lens in the Y axis shows a similar degree of shift in beam center position across d_{va} than PCI-D-PM$_{2.5}$ while the shift in the X axis is less variable than that of PCI-D-PM$_{2.5}$. However, since the PM$_{2.5}$ lens was not installed in the same rotational orientation, it is not appropriate to conclude that the use of PCI-D magnifies the shifts in beam center positions.
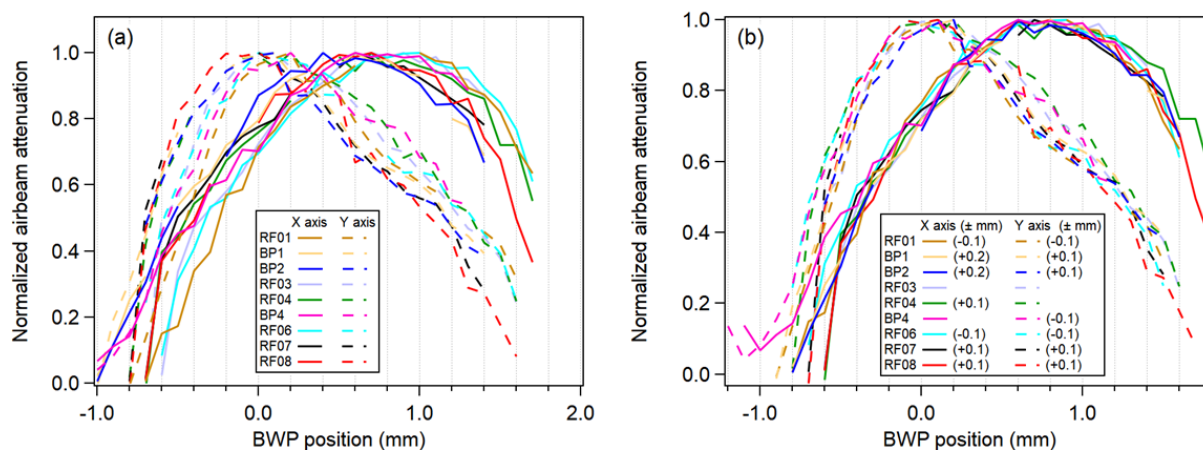
Figure S16.2. (a) Air beam (AB) signal with the default offset correction (-0.5 mm in X axis, -0.6 mm in Y axis). (b) The same graph with additional corrections (within ± 0.2 mm) for better alignment in the air beam profile. Careful inspection of the BWP AB recorded at high resolution for many runs revealed what appears to be inconsistent zeroing of the BWP in the control software, with a maximum variability of 0.2 mm. Hence all data shown here has been corrected using the BWP AB as datum.

S17. Aircraft inlet logs during the TI³GER campaign
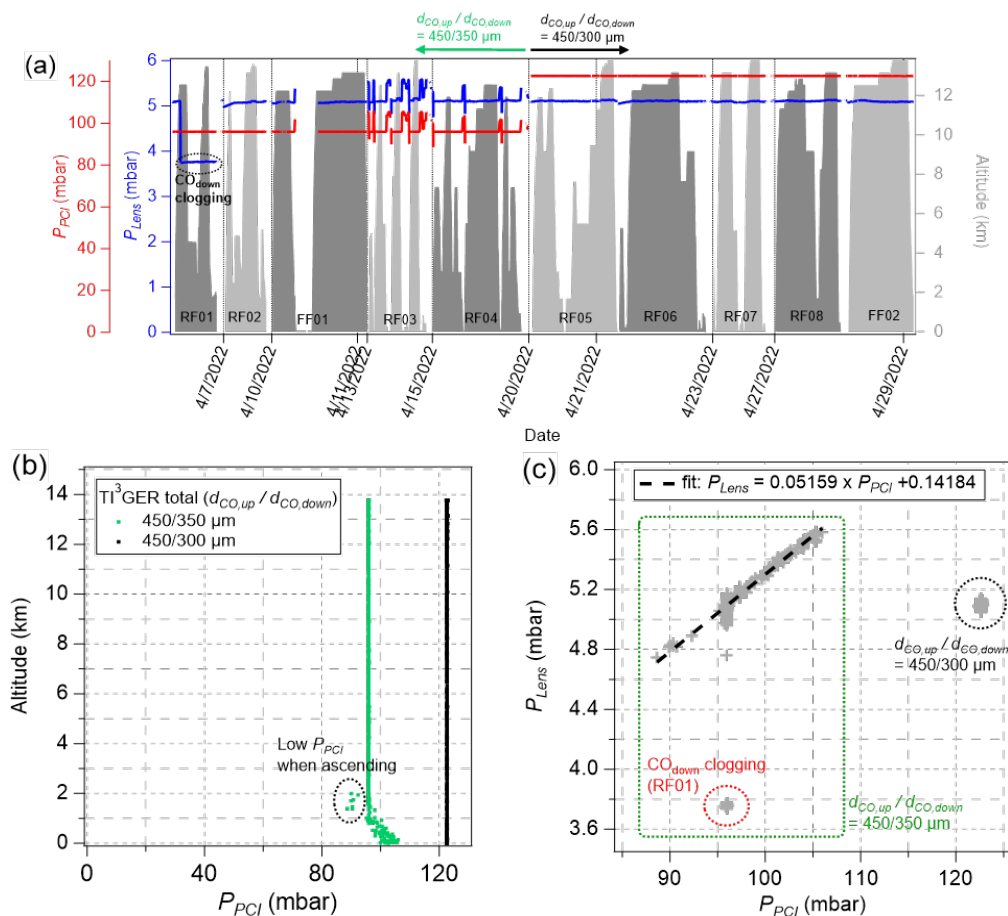
Figure S17.1. (a) Time series of P_{PCI}, P_{Lens}, and altitude. The CO_{down} clogging (RF01) occurred ~ 40 minutes after the flight and was resolved during landing (before IE calibration & 1D-BWPs). The CO_{up}/CO_{down} configuration of PCI-D was 450/350 µm (P_{PCI} = 96 mbar) during RF01-RF04 & FF01 (ferry flight from Colorado to Hawaii) and 450/300 µm (P_{PCI} = 122.6 mbar) for RF05-RF08 & FF02 (ferry flight from Hawaii to Colorado). The PCI-D of both critical orifice configurations successfully maintained the constant P_{PCI} at high altitudes during the campaign (maximum ~ 13.8 km). The 450/350 µm configuration failed to maintain the constant P_{PCI} below 1.6 km altitude due to the pressure drop at the PCI flowmeter and the limitation in pumping capacity of the PCI pump. This increased the P_{Lens} up to 5.7 mbar at sea level. The increased P_{Lens} (~ 10%) might have affected the $d_{va,50,low}$ negatively but not significantly (Fig. S13.1). (b) Altitude vs. P_{PCI} for both critical orifice configurations. In the 450/350 µm configuration, the PCI pumping control did not work smoothly when G-V was ascending above 1 km altitude, resulting in lower P_{PCI} than the set value. (c) P_{Lens} vs. P_{PCI}. In 450/350 µm configuration, P_{Lens} responded linearly to the higher (below 1.6 km altitude) and lower (ascending above 1 km altitude) P_{PCI} than the set P_{PCI}.
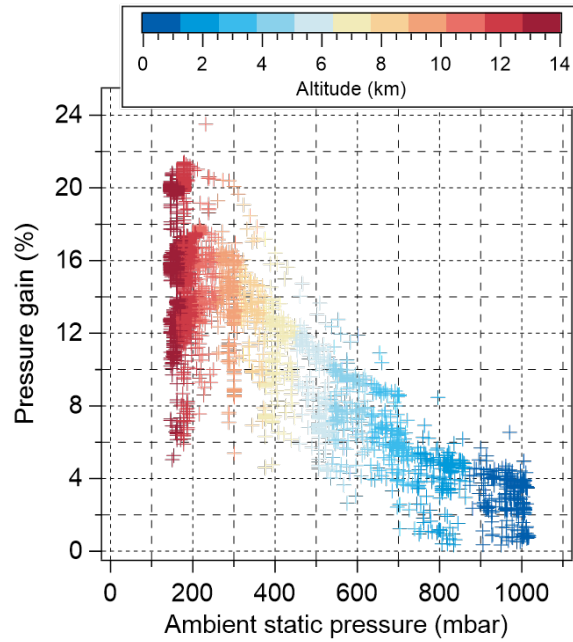
Figure S17.2. The optimal operation altitude ranges in Fig. 15d were calculated as an altitude at which ambient pressure is equal to P_{PCI} without considering the pressure gain due to ram pressure. The measured pressure gain due to the ram pressure during the flight as a function of ambient pressure is shown here, following Pressure gain (%) = 100 x (sampling line pressure downstream of HIMIL - ambient static pressure) / ambient static pressure. This means that with CU-AMS inlet configuration during TI³GER on G-V, the actual optimal altitude range is ~ 1 km higher.

S18. Particle transmission through sampling lines during TI³GER
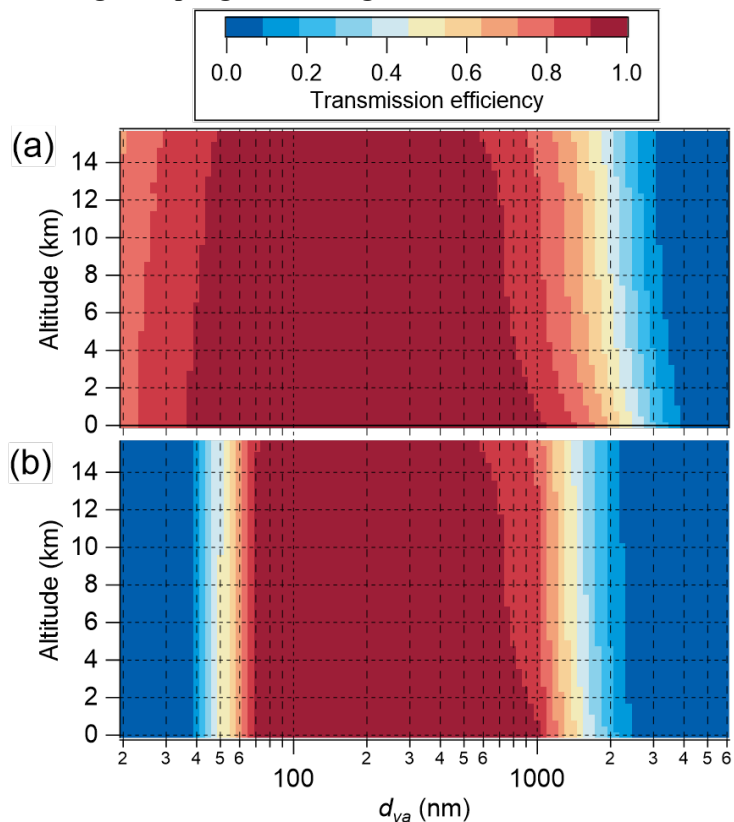
450 **Figure S18.1.** Calculated aerosol transmission through (a) the plumbing upstream of PCI and (b) the whole inlet (including PCI-D-PM$_{2.5}$) as a function of altitude. In addition to the particle losses in PCI and ADL, particles are lost in the sampling lines downstream of the tip of the secondary diffuser, while there are small particle concentration effects at the takeoffs. Losses in the HIMIL (before the secondary diffuser) were not included. Calculations were performed with a custom fluid-dynamics equation package, as described in Guo et al. (2021) and Bourgeois et al. (2022).

455

S19. Aerosol quantification of UHSAS during TI³GER
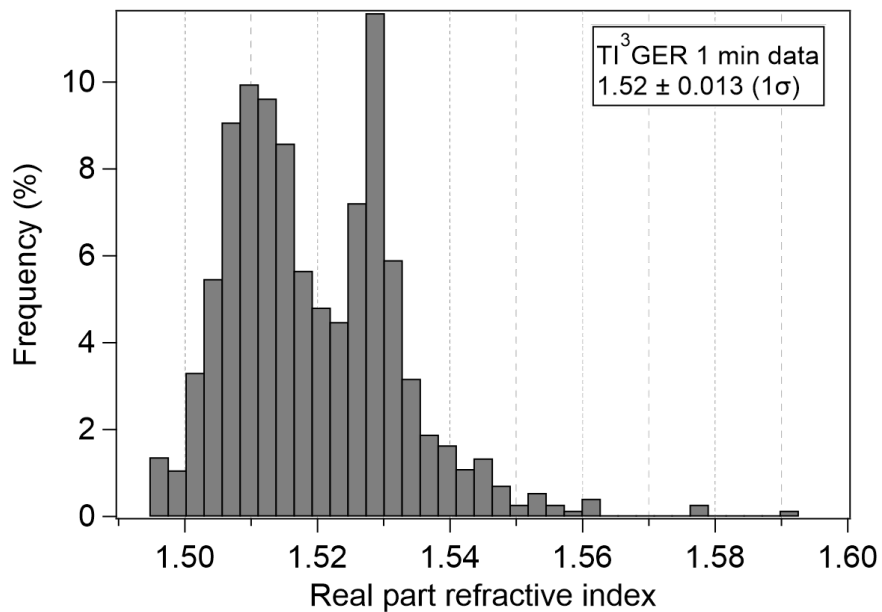
Figure S19.1. Histogram of the estimated real part of the refractive index of the particles sampled during the TI³GER campaign
460 (see Sect. 2.6.2 for a description of the method).
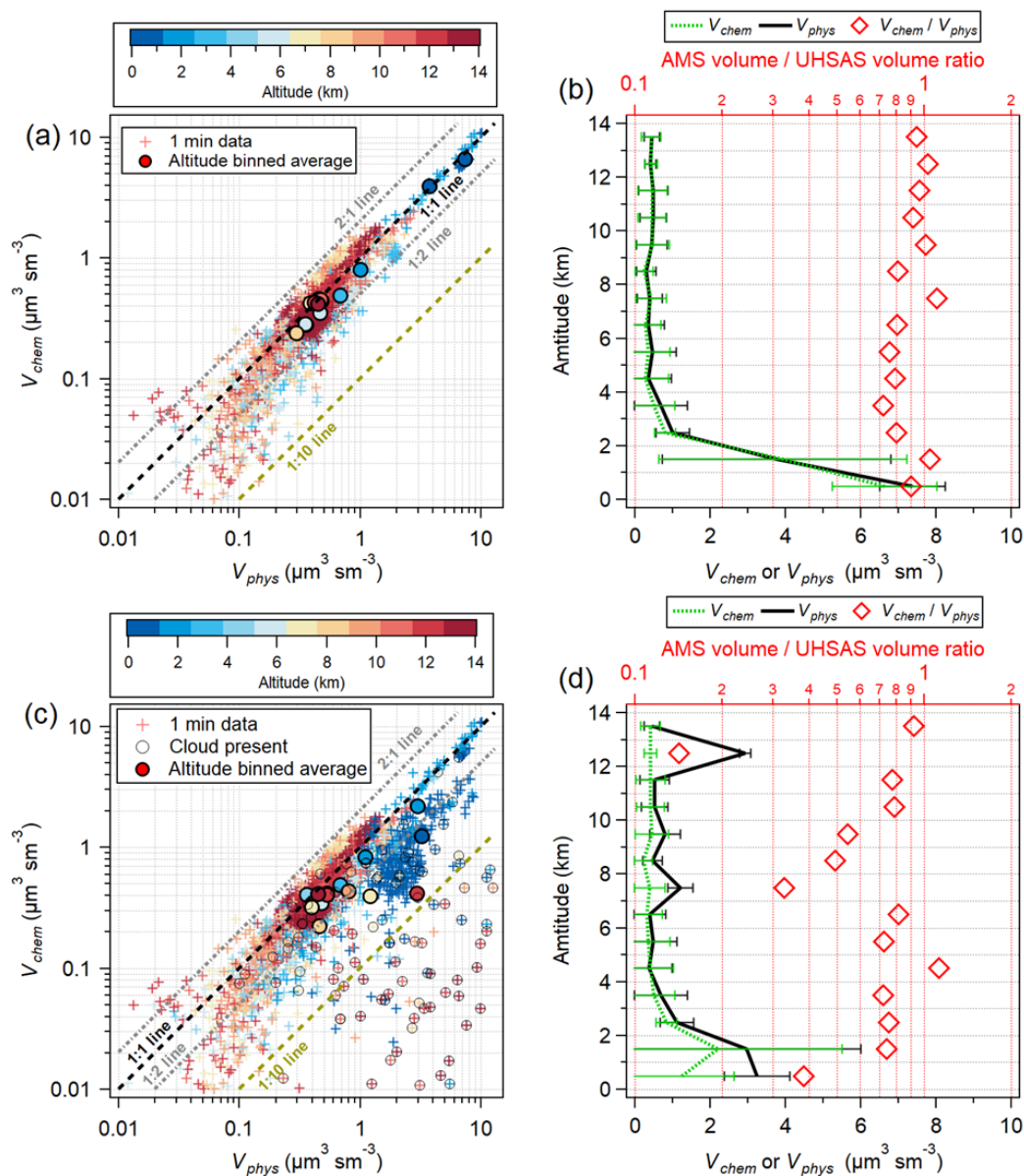
Figure S19.2. Aerosol volume concentrations measured by AMS (V_{chem}) vs. by UHSAS (RI-corrected, V_{phys}) as a function of altitude. (a-b) Aerosol volume comparison excluding data with the presence of cloud particles (identified by cloud droplet probe) in log scale (see Fig. 17b for linear scale). (c-d) Aerosol volume comparison with all data.

S20. Post-campaign characterization of air slowdown inside the HIAPER Modular Inlet (HIMIL)

470   HIAPER Modular Inlet (HIMIL) (Fig. 2 and Fig. S20.1) is a flow-through inlet facing flight direction with a diffusing nozzle upstream and a converging nozzle downstream which is broadly used for in-situ sampling on research aircraft (Stith et al., 2009) They are typically flown with a choice of two spacers, a standard one (19 cm above the fuselage) and a tall one (29.5 cm above the fuselage), the one used for both the TI3GER AMS sampling and the characterization here is the latter one, with less chance of boundary layer contamination. The HIMIL is used both for gas-phase and particle-phase species, with the gas-

475   phase version using a larger nozzle ID (½" vs ⅜") and an active choke on the exhaust; these measurements focus on the original version optimized for aerosols. As a sharp-edged diffuser inlet, the HIMIL that could potentially exhibit directional losses for larger particles (Baumgardner and Huebert, 1993). During the Pacific Dust Experiment (PACDEX) four HIMILs were deployed. The calculated particle passing efficiencies of approximately 94 to 110% for particles 1 μm diameter and smaller, over the range of typical G-V sampling altitudes (sea level to 12 km) and airspeeds (120–260 m s^{-1}) (Stith et al., 2009).

480   Several cross-comparisons of aerosol measurements between HIMIL and different types of inlets such as Blunt-body Aerosol Sampler (Moharreri et al., 2013), Submicron Aerosol Inlet (Ortega et al., 2019), and NASA Langley Aerosol Research Group inlet (Guo et al., 2021) have been reported. Guo et al. (2021) showed that using a completely different inlet with proven supermicron transmission (McNaughton et al., 2007; Brock et al., 2019) while maintaining the same conditions in the downstream plumbing, had no appreciable impact on the intercomparisons with other optical aerosol instruments during back-

485   to-back inlet switches. However, to the best of our knowledge, there has been no experimental characterization of the HIMIL inlet itself. Since quantitative, unbiased sampling thru the secondary diffuser using for AMS operation depends on roughly matching the flow speed in the HIMIL and the secondary diffuser, the air slowdown factor of the HIMIL (or the air speed inside HIMIL) at each altitude needs to be known. An estimated slowdown of ambient air from plane airspeed by a factor of 3-4 inside the diffuser has been suggested (D. Rogers, NCAR, personal communication) while assuming laminar flow

490   expansion in the diffuser would suggest a slowdown factor as high as 11.75.

    For TI^{3}GER, the flow is then sampled into a straight, sharp-edged 3.8 mm internal diameter (ID) stainless steel tube pointing in the flow direction (called here the "secondary diffuser") (Guo et al., 2021). The small particle losses through the HIMIL and secondary diffuser are negligible due to fast residence time. Large particle (~ 1 μm diameter) transmission can be affected by the particle transmission through the tip of the HIMIL as the air slows down (passing efficiency),

495   over/undersampling at the tip of the secondary diffuser depending on the flowrate at the secondary diffuser, and the impaction loss in the particle sampling line downstream of the secondary diffuser. The particle impaction at the 90-degree bend at the secondary diffuser inside HIMIL (Fig. S20.1) is the largest loss, especially for larger particles. Thus, reducing the flow rate at the secondary diffuser, while maintaining near isokinetic sampling at the secondary diffuser is the key to enhancing large particle transmission.

500   The objective of the characterization in this section is to evaluate the flow velocity along the centerpiece of the HIMIL (where the secondary inlet is normally placed), in order a) to determine to what extent flow speeds are slowed down in the

HIMIL compared to the ambient flow speed and b) to evaluate the symmetry of the flow profile and the likelihood of flow separation (or "jetting"). In this section, we present the airspeed measurements inside HIMIL as a function of height and its dependency on the angle of attack at the U.S. Air Force Academy (USAFA). Airspeed was calculated based on the measured ram pressure (or stagnation pressure, P_t) from a (ID: 1.34 mm, OD: 1/16") and static pressure (P_s) measured at the HIMIL inside wall, following Eq. S20.1 which is valid for Mach numbers < 0.3 (measured flow velocities inside the HIMIL were <0.1 Mach).

$$u = \sqrt{\frac{2(P_t - P_s)}{\rho_{air}}} \, , \hspace{4cm} \text{(Eq. S20.1)}$$

where u is the speed of air and ρ_{air} is the density of air after being corrected by temperature and pressure. The air speed inside HIMIL over a range of external air speeds was measured at three pitot tube locations (referred to as front, middle, and back positions; Fig. S20.2a).

During the wind tunnel experiments at USAFA, a pressure sensor (KMPS-4-64-XX-Y series, Kulite Inc.), acquiring at 250 Hz sample rate, was used for differential pressure measurements. The full vertical profiles of air speed inside the HIMIL over a range of wind tunnel air speeds were measured at the front, middle, and back locations. Four wind speeds (100 m s^{-1}, 125 m s^{-1}, 150 m s^{-1}, and 180 m s^{-1}) were chosen for the vertical profile measurements to cover the range of typical airspeeds at the HIMIL tip from various aircraft research platforms (NSF GV, NSF C130, NASA DC-8) while probing the lower 5 km of the atmosphere. Given the limitations of the tunnel (ambient T and P, max Mach number of 0.55), these experiments do not cover conditions in the upper troposphere and stratosphere (Fig. S20.3). Before each vertical profile measurement, the pitot tube was placed at the center height measuring the HIMIL internal air speed as the wind tunnel air speed increase by ~ 10 m s^{-1} step ("speed run"). After the wind tunnel air speed reached the maximum speed (180 m s^{-1}), the wind tunnel air speed slowed down to the four selected speeds and the pitot tube height measured the airspeed profile at each speed. Measurement at each speed was averaged for 5-10 s. Up to 180 m s^{-1} (Mach 0.52), flow separation (or "jetting") was not observed, although the airspeed vertical profile was asymmetric in the front position (Fig. S20.4a) (this could partially be related to a slight deformation to the front cone during the experiments, see Fig. 20.2c). The symmetry of the vertical profile is achieved as the air travels further back (Fig. S20.4b-c). The "speed run" data at the three pitot positions shows that the air speed slowdown ratio of the HIMIL is about a factor of 7.4 (Fig. S20.4d) at the position of the tip of the secondary diffuser. The air speed decreased towards the back of the HIMIL by ~ 35%, almost approaching the full expansion value. The reason behind the airspeed slowdown in the back side of HIMIL could not be conclusively assessed. On the other hand, the static pressure measurements on the front, middle, and back positions were nearly identical indicating the air speed would have been similar among the three locations. This discrepancy will be investigated in future studies. Leaks around HIMIL component fittings were not found. The air speed inside HIMIL decreased as the pitch angle deviated from 0 degree, up to ~ 15 % (at +7 degrees; Fig. S20.5).

During the TI^{3}GER campaign, the air speed at the tip of the secondary diffuser (determined by the flow rate) was faster than the air speed around the tip (estimated by the wind tunnel data, grey marker, Fig. S20.6). From the extrapolation of

535 the wind tunnel data, this indicates that there may have been a minor degree of undersampling of particles near ~ 1 µm volume

equivalent diameter (d_{ve}) by the secondary diffuser, although the flow field during actual flight conditions (low temperature

and pressure) could deviate from the extrapolation. However, such undersampling is minor and the contribution of particles

with ~ 1 µm d_{ve} (~ 1.6 µm d_{va}) to mass in accumulation mode aerosols is a small fraction (Fig. 17). Thus, this effect does not

meaningfully affect aerosol quantification compared to the particle losses in the sampling line downstream of the secondary

540 diffuser. In future campaigns, the sampling flow rate from the secondary diffuser can be adjusted to minimize the particle

losses in the sampling downstream of the secondary diffuser while achieving near isokinetic sampling.
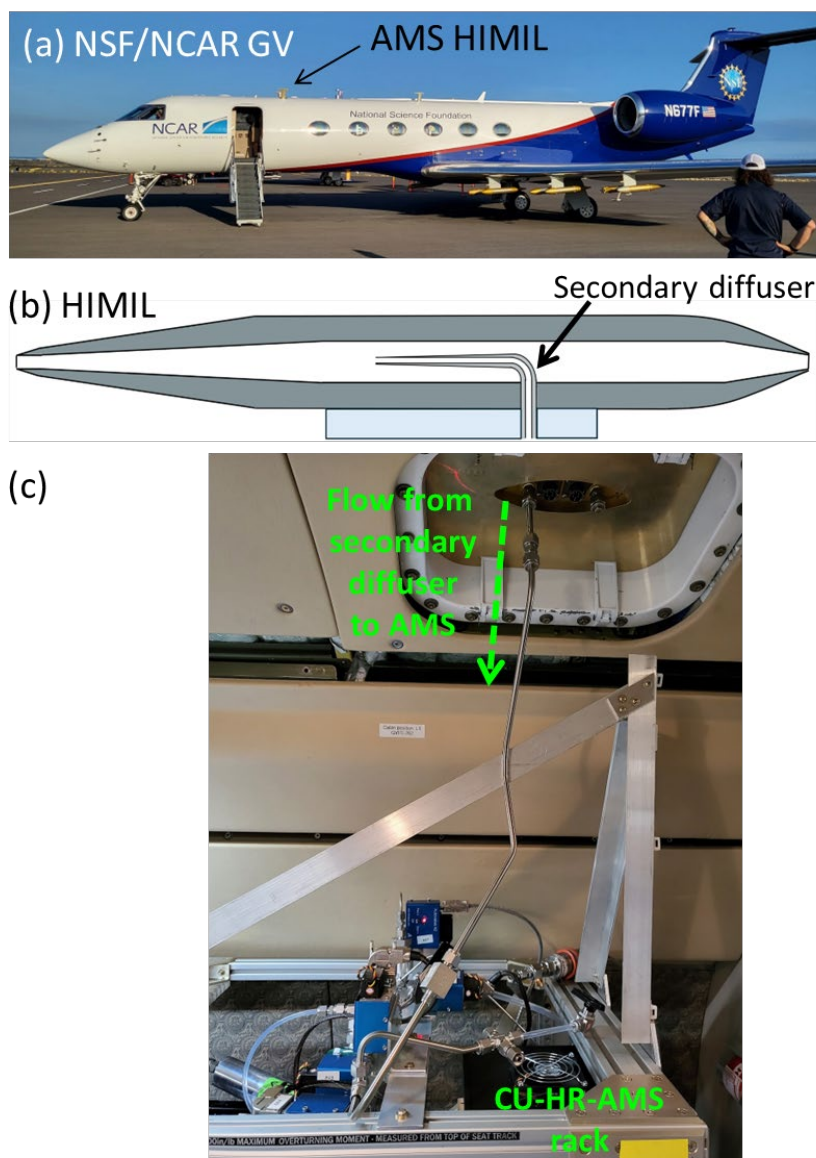
Figure S20.1. (a) Location of HIMIL for CU-HR-AMS on GV. (b) Cross section of HIMIL and the location of the secondary diffuser. (c) Aerosol sampling line downstream of the secondary diffuser.
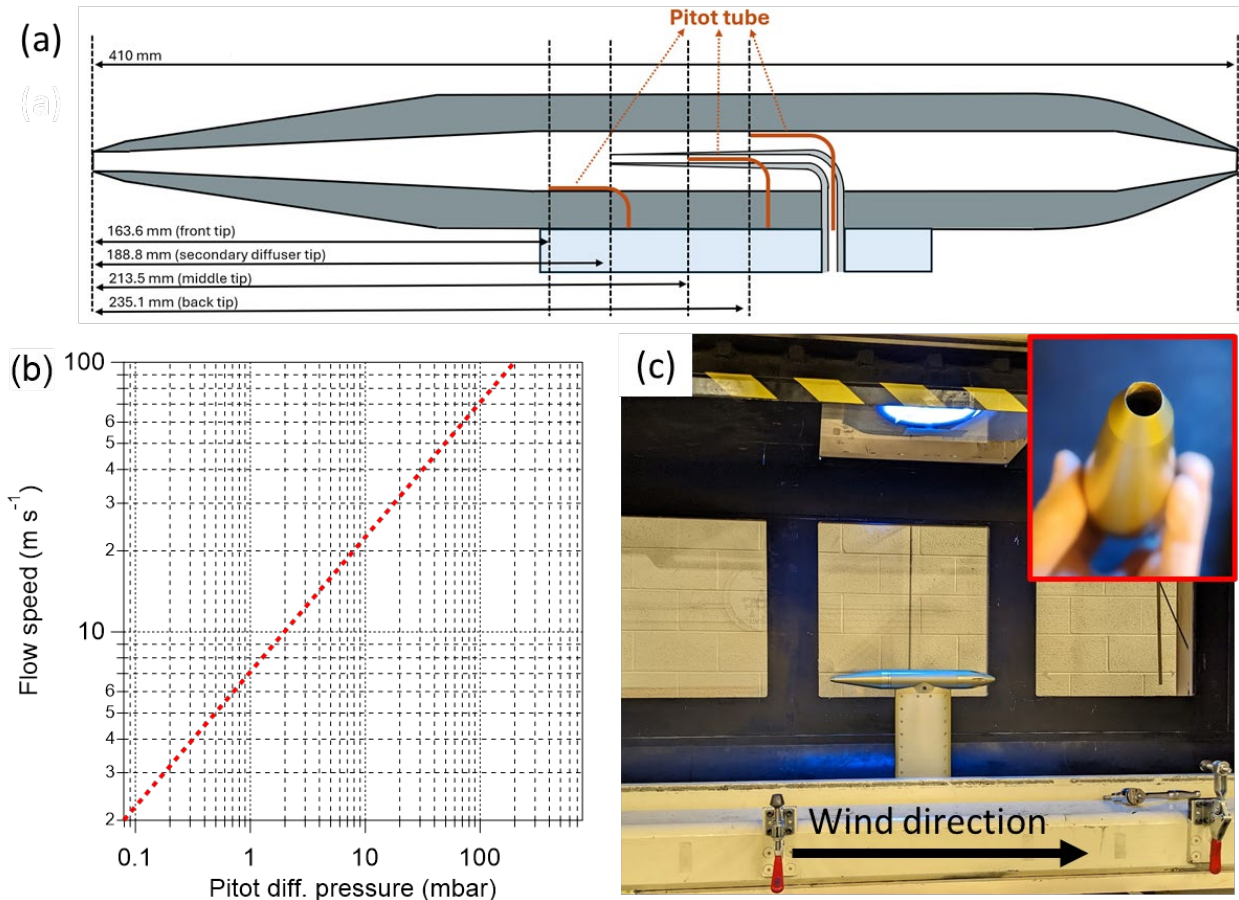
Figure S20.2. (a) Locations of three pitot tube positions (front, middle, and back) inside HIMIL. When conducting ram pressure measurement at one pitot tube position, another port is used for static pressure measurement and the other port is blocked. (b) The relationship between the measured differential pitot pressure and the flow speed (Eq. S20.1). (c) HIMIL installed inside the wind tunnel at the U.S. Air Force Academy. The inset picture in red box shows the slightly deformed front cone of the HIMIL tested and deployed during the TI^{3}GER.
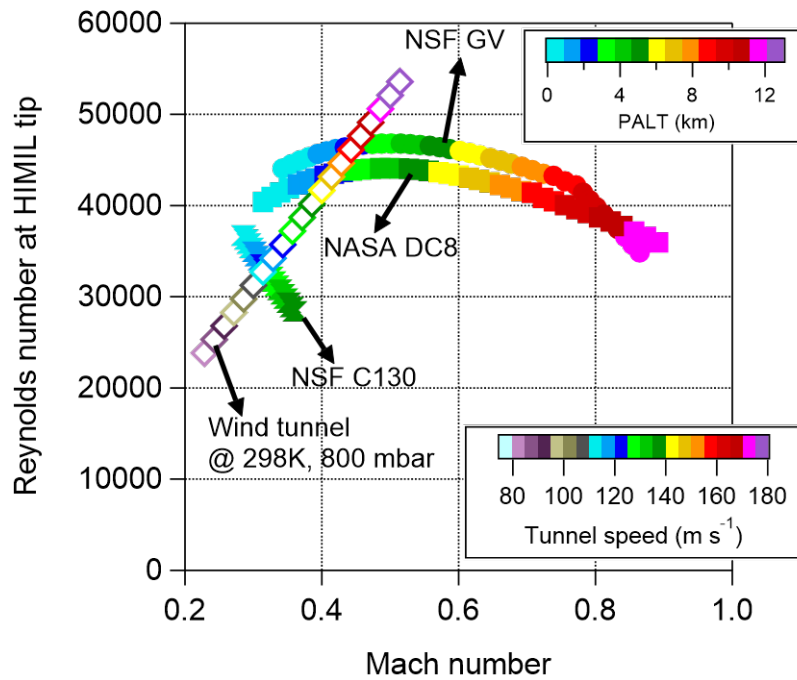
560 **Figure S20.3.** Reynolds number at the HIMIL tip vs Mach number for the polar of different aircraft platforms compared to the range of conditions accessible by the wind tunnel. The wind tunnel condition overlap with the inlet conditions of research aircraft at lower altitudes (below ~5 km). This suggests that the HIMIL experiment with wind tunnel is more representative of low altitude condition and, at higher altitude, the wind tunnel result on air speed slowdown could deviate from research flight conditions.

565

570
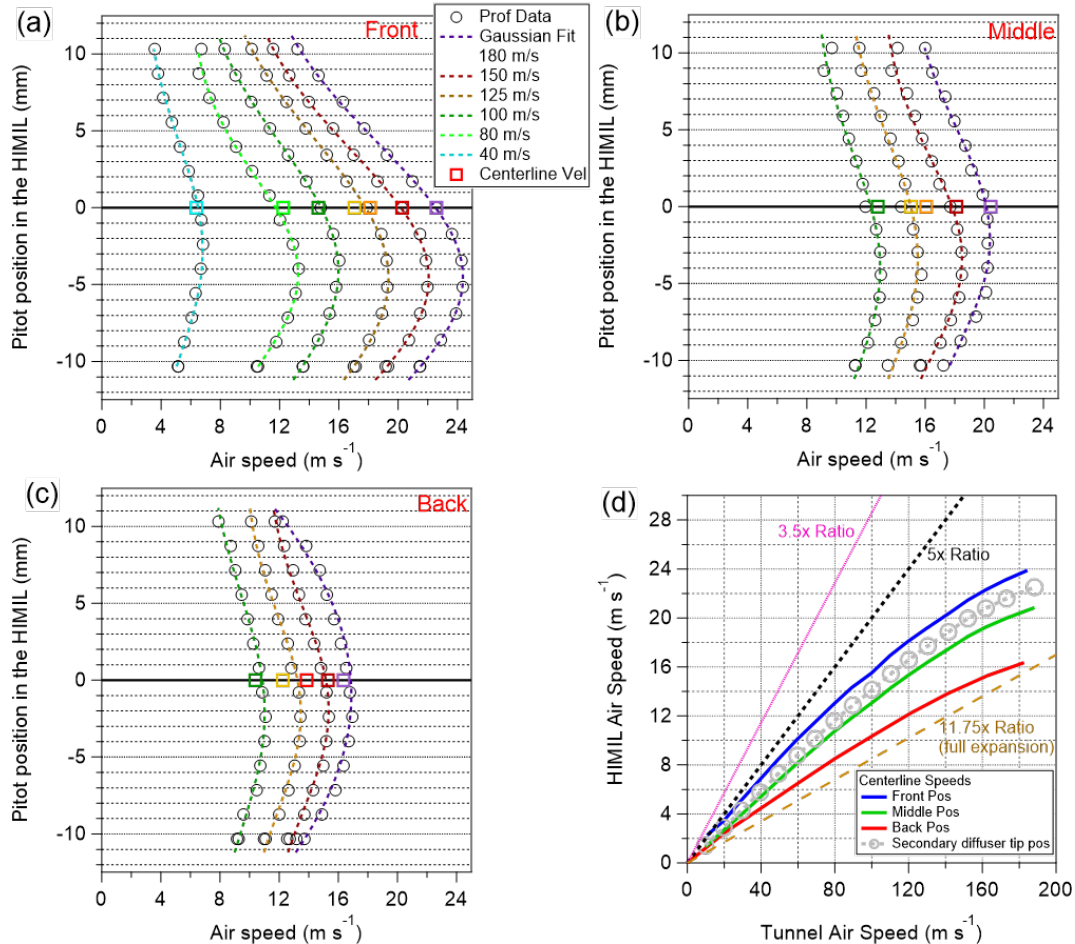
575

Figure S20.4. The wind tunnel measurement of air speed vertical profile inside HIMIL at (a) front, (b) middle, (c) back positions. Centerline velocity is air speed measured during the continuous "speed run" cycle at the same tunnel air speed where profile measurements were conducted. The fact that the air speed from profiles and "speed run" agree indicates that the air speed measurement is reproducible. (d) HIMIL air speed vs tunnel air speed at the front, middle, and back pitot positions at

580 the center height. HIMIL air speed decreased toward the back side of HIMIL. Gray markers are the estimated HIMIL air speed at the location of the tip of the secondary diffuser.
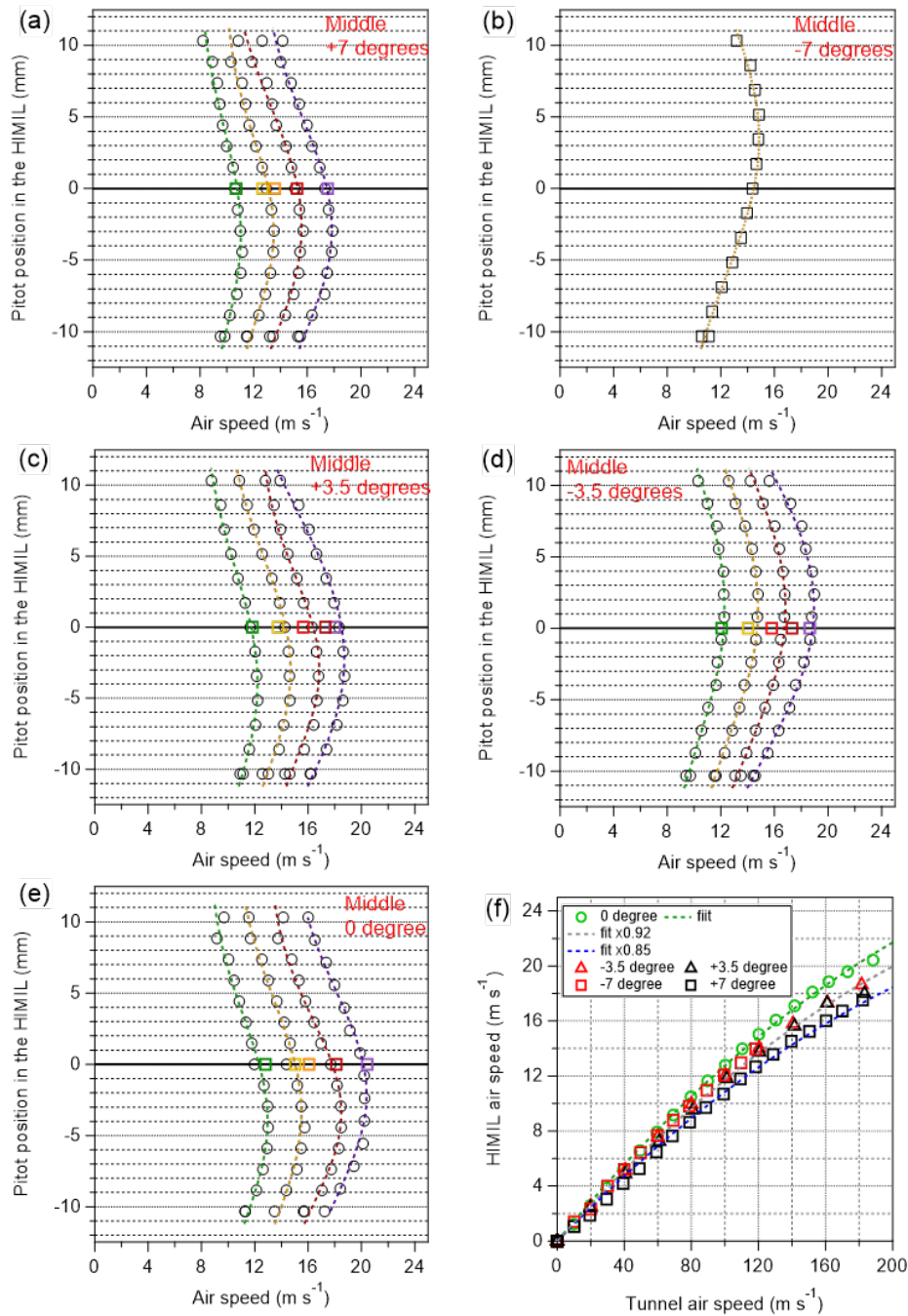
Figure S20.5. The wind tunnel measurement of airspeed profile inside HIMIL at different pitch angles for the middle pitot position. Profiles of 0, +3.5, +7.5 degrees are skewed towards the bottom by similar amounts. The +7 deg pitch is noticeably slower than 0 deg (by ~ 15 %). -7.5 deg on the other hand looks like expected. The overall effect on air speed, especially for realistic pitch angles (e.g. -3.5 to +3.5 deg) is modest (within ~ 8 %).

585
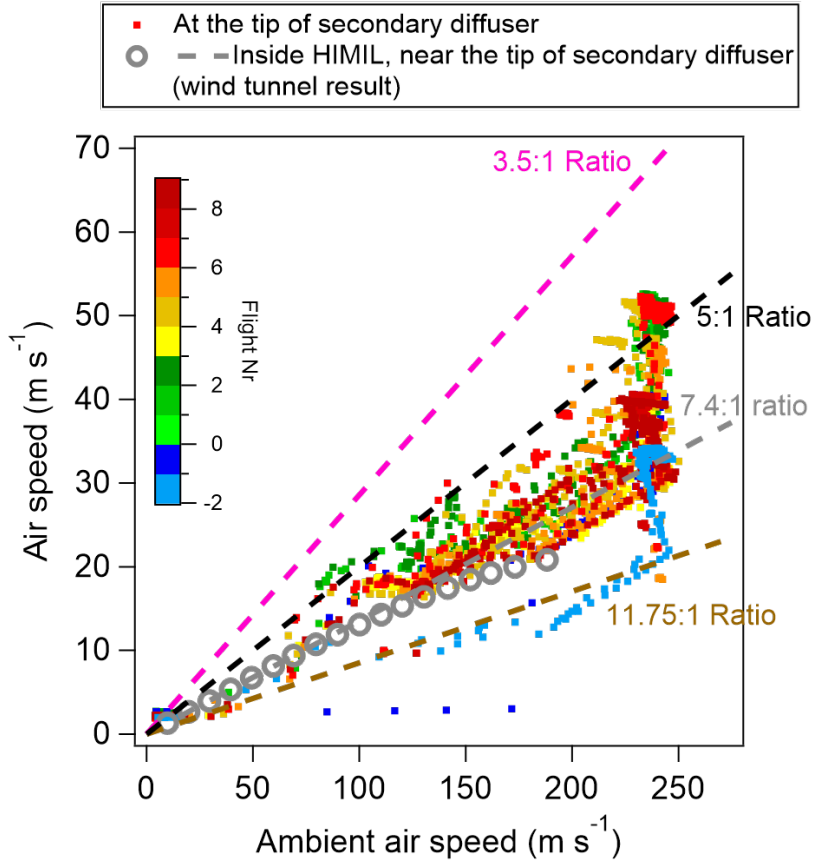
Figure S20.6. The calculated air intake speed at the tip of the secondary diffuser during the TI³GER campaign and the extrapolated air speed inside the HIMIL at the location of the tip of the secondary diffuser from the wind tunnel experiment.

References

Alfarra, M.: Insights Into Atmospheric Organic Aerosols Using an Aerosol Mass Spectrometer, Ph.D. thesis, University of Manchester., 2004.

595 Bahreini, R., Dunlea, E. J., Matthew, B. M., Simons, C., Docherty, K. S., DeCarlo, P. F., Jimenez, J. L., Brock, C. A. and Middlebrook, A. M.: Design and Operation of a Pressure-Controlled Inlet for Airborne Sampling with an Aerodynamic Aerosol Lens, Aerosol Sci. Technol., 42(6), 465–471, 2008.

Baumgardner, D. and Huebert, B.: The airborne aerosol inlet workshop: Meeting report, J. Aerosol Sci., 24(6), 835–846, 1993.

Bourgeois, I., Peischl, J., Neuman, J. A., Brown, S. S., Allen, H. M., Campuzano-Jost, P., Coggon, M. M., DiGangi, J. P.,
600 Diskin, G. S., Gilman, J. B., Gkatzelis, G. I., Guo, H., Halliday, H. A., Hanisco, T. F., Holmes, C. D., Huey, L. G., Jimenez, J. L., Lamplugh, A. D., Lee, Y. R., Lindaas, J., Moore, R. H., Nault, B. A., Nowak, J. B., Pagonis, D., Rickly, P. S., Robinson, M. A., Rollins, A. W., Selimovic, V., St. Clair, J. M., Tanner, D., Vasquez, K. T., Veres, P. R., Warneke, C., Wennberg, P. O., Washenfelder, R. A., Wiggins, E. B., Womack, C. C., Xu, L., Zarzana, K. J. and Ryerson, T. B.: Comparison of airborne measurements of NO, NO_2, HONO, NO_y, and CO during FIREX-AQ, Atmos. Meas. Tech., 15(16), 4901–4930, 2022.

605 Brock, C. A., Williamson, C., Kupc, A., Froyd, K. D., Erdesz, F., Wagner, N., Richardson, M., Schwarz, J. P., Gao, R.-S., Katich, J. M., Campuzano-Jost, P., Nault, B. A., Schroder, J. C., Jimenez, J. L., Weinzierl, B., Dollner, M., Bui, T. and Murphy, D. M.: Aerosol size distributions during the Atmospheric Tomography Mission (ATom): methods, uncertainties, and data products, Atmos. Meas. Tech., 12(6), 3081–3099, 2019.

Canagaratna, M. R., Jimenez, J. L., Kroll, J. H., Chen, Q., Kessler, S. H., Massoli, P., Hildebrandt Ruiz, L., Fortner, E.,
610 Williams, L. R., Wilson, K. R., Surratt, J. D., Donahue, N. M., Jayne, J. T. and Worsnop, D. R.: Elemental ratio measurements of organic compounds using aerosol mass spectrometry: characterization, improved calibration, and implications, Atmos. Chem. Phys., 15(1), 253–272, 2015.

Crenn, V., Sciare, J., Croteau, P. L., Verlhac, S., Fröhlich, R., Belis, C. A., Aas, W., Äijälä, M., Alastuey, A., Artiñano, B., Baisnée, D., Bonnaire, N., Bressi, M., Canagaratna, M., Canonaco, F., Carbone, C., Cavalli, F., Coz, E., Cubison, M. J., Esser-
615 Gietl, J. K., Green, D. C., Gros, V., Heikkinen, L., Herrmann, H., Lunder, C., Minguillón, M. C., Močnik, G., O'Dowd, C. D., Ovadnevaite, J., Petit, J.-E., Petralia, E., Poulain, L., Priestman, M., Riffault, V., Ripoll, A., Sarda-Estève, R., Slowik, J. G., Setyan, A., Wiedensohler, A., Baltensperger, U., Prévôt, A. S. H., Jayne, J. T. and Favez, O.: ACTRIS ACSM intercomparison – Part 1: Reproducibility of concentration and fragment results from 13 individual Quadrupole Aerosol Chemical Speciation Monitors (Q-ACSM) and consistency with co-located instruments, Atmos. Meas. Tech., 8(12), 5063–5087, 2015.

620 Day, D. A., Fry, J. L., Kang, H. G., Krechmer, J. E., Ayres, B. R., Keehan, N. I., Thompson, S. L., Hu, W., Campuzano-Jost, P., Schroder, J. C., Stark, H., DeVault, M. P., Ziemann, P. J., Zarzana, K. J., Wild, R. J., Dubè, W. P., Brown, S. S. and Jimenez, J. L.: Secondary organic aerosol mass yields from NO3 oxidation of α-pinene and Δ-Carene: Effect of RO2 radical fate, J. Phys. Chem. A, 126(40), 7309–7330, 2022.

DeCarlo, P. F., Dunlea, E. J., Kimmel, J. R., Aiken, A. C., Sueper, D., Crounse, J., Wennberg, P. O., Emmons, L., Shinozuka,
625 Y., Clarke, A., Zhou, J., Tomlinson, J., Collins, D. R., Knapp, D., Weinheimer, A. J., Montzka, D. D., Campos, T. and Jimenez, J. L.: Fast airborne aerosol size and chemistry measurements above Mexico City and Central Mexico during the MILAGRO campaign, Atmos. Chem. Phys., 8(14), 4027–4048, 2008.

Drewnick, F., Diesch, J.-M., Faber, P. and Borrmann, S.: Aerosol mass spectrometry: particle–vaporizer interactions and their consequences for the measurements, Atmospheric Measurement Techniques, 8(9), 3811–3830, 2015.

630 Dunlea, E. J., DeCarlo, P. F., Aiken, A. C., Kimmel, J. R., Peltier, R. E., Weber, R. J., Tomlinson, J., Collins, D. R., Shinozuka, Y., McNaughton, C. S., Howell, S. G., Clarke, A. D., Emmons, L. K., Apel, E. C., Pfister, G. G., van Donkelaar, A., Martin,

R. V., Millet, D. B., Heald, C. L. and Jimenez, J. L.: Evolution of Asian aerosols during transpacific transport in INTEX-B, Atmos. Chem. Phys., 9(19), 7257–7287, 2009.

635 Guo, H., Campuzano-Jost, P., Nault, B. A., Day, D. A., Schroder, J. C., Kim, D., Dibb, J. E., Dollner, M., Weinzierl, B. and Jimenez, J. L.: The importance of size ranges in aerosol instrument intercomparisons: a case study for the Atmospheric Tomography Mission, Atmospheric Measurement Techniques, 14(5), 3631–3655, 2021.

Hu, W., Campuzano-Jost, P., Day, D. A., Croteau, P., Canagaratna, M. R., Jayne, J. T., Worsnop, D. R. and Jimenez, J. L.: Evaluation of the new capture vapourizer for aerosol mass spectrometers (AMS) through laboratory studies of inorganic species, Atmos. Meas. Tech., 10(8), 2897–2921, 2017.

640 Hu, W., Day, D. A., Campuzano-Jost, P., Nault, B. A., Park, T., Lee, T., Croteau, P., Canagaratna, M. R., Jayne, J. T., Worsnop, D. R. and Jimenez, J. L.: Evaluation of the New Capture Vaporizer for Aerosol Mass Spectrometers (AMS): Elemental Composition and Source Apportionment of Organic Aerosols (OA), ACS Earth Space Chem., 2(4), 410–421, 2018a.

Hu, W., Day, D. A., Campuzano-Jost, P., Nault, B. A., Park, T., Lee, T., Croteau, P., Canagaratna, M. R., Jayne, J. T., Worsnop, D. R. and Jimenez, J. L.: Evaluation of the new capture vaporizer for aerosol mass spectrometers: Characterization of organic 645 aerosol mass spectra, Aerosol Sci. Technol., 52(7), 725–739, 2018b.

Jayne, J. T., Leard, D. C., Zhang, X., Davidovits, P., Smith, K. A., Kolb, C. E. and Worsnop, D. R.: Development of an Aerosol Mass Spectrometer for Size and Composition Analysis of Submicron Particles, Aerosol Sci. Technol., 33(1-2), 49–70, 2000.

Katz, E. F., Guo, H., Campuzano-Jost, P., Day, D. A., Brown, W. L., Boedicker, E., Pothier, M., Lunderberg, D. M., Patel, S., Patel, K., Hayes, P. L., Avery, A., Hildebrandt Ruiz, L., Goldstein, A. H., Vance, M. E., Farmer, D. K., Jimenez, J. L. and 650 DeCarlo, P. F.: Quantification of cooking organic aerosol in the indoor environment using aerodyne aerosol mass spectrometers, Aerosol Sci. Technol., 55(10), 1099–1114, 2021.

Knote, C., Brunner, D., Vogel, H., Allan, J., Asmi, A., Äijälä, M., Carbone, S., van der Gon, H. D., Jimenez, J. L., Kiendler-Scharr, A., Mohr, C., Poulain, L., Prévôt, A. S. H., Swietlicki, E. and Vogel, B.: Towards an online-coupled chemistry-climate model: evaluation of trace gases and aerosols in COSMO-ART, Geosci. Model Dev., 4(4), 1077–1102, 2011.

655 Krechmer, J. E., Day, D. A., Ziemann, P. J. and Jimenez, J. L.: Direct Measurements of Gas/Particle Partitioning and Mass Accommodation Coefficients in Environmental Chambers, Environ. Sci. Technol., 51(20), 11867–11875, 2017.

Liu, P. S. K., Deng, R., Smith, K. A., Williams, L. R., Jayne, J. T., Canagaratna, M. R., Moore, K., Onasch, T. B., Worsnop, D. R. and Deshler, T.: Transmission Efficiency of an Aerodynamic Focusing Lens System: Comparison of Model Calculations and Laboratory Measurements for the Aerodyne Aerosol Mass Spectrometer, Aerosol Sci. Technol., 41(8), 721–733, 2007.

660 Matthew, B. M., Middlebrook, A. M. and Onasch, T. B.: Collection Efficiencies in an Aerodyne Aerosol Mass Spectrometer as a Function of Particle Phase for Laboratory Generated Aerosols, Aerosol Sci. Technol., 42(11), 884–898, 2008.

McNaughton, C. S., Clarke, A. D., Howell, S. G., Pinkerton, M., Anderson, B., Thornhill, L., Hudgins, C., Winstead, E., Dibb, J. E., Scheuer, E. and Maring, H.: Results from the DC-8 Inlet Characterization Experiment (DICE): Airborne Versus Surface Sampling of Mineral Dust and Sea Salt Aerosols, Aerosol Sci. Technol., 41(2), 136–159, 2007.

665 Moharreri, A., Craig, L., Rogers, D. C. and Dhaniyala, S.: A New Aircraft Inlet for Sampling Interstitial Aerosol: Design Methodology, Modeling, and Wind Tunnel Tests, Aerosol Sci. Technol., 47(8), 885–894, 2013.

Molleker, S., Helleis, F., Klimach, T., Appel, O., Clemen, H.-C., Dragoneas, A., Gurk, C., Hünig, A., Köllner, F., Rubach, F., Schulz, C., Schneider, J. and Borrmann, S.: Application of an O-ring pinch device as a constant-pressure inlet (CPI) for airborne sampling, Atmos. Meas. Tech., 13(7), 3651–3660, 2020.

670 Nault, B. A., Campuzano-Jost, P., Day, D. A., Schroder, J. C., Anderson, B., Beyersdorf, A. J., Blake, D. R., Brune, W. H., Choi, Y., Corr, C. A., de Gouw, J. A., Dibb, J., DiGangi, J. P., Diskin, G. S., Fried, A., Huey, L. G., Kim, M. J., Knote, C. J., Lamb, K. D., Lee, T., Park, T., Pusede, S. E., Scheuer, E., Thornhill, K. L., Woo, J.-H. and Jimenez, J. L.: Secondary organic aerosol production from local emissions dominates the organic aerosol budget over Seoul, South Korea, during KORUS-AQ, Atmos. Chem. Phys., 18(24), 17769–17800, 2018.

675 Nault, B. A., Croteau, P., Jayne, J., Williams, A., Williams, L., Worsnop, D., Katz, E. F., DeCarlo, P. F. and Canagaratna, M.: Laboratory evaluation of organic aerosol relative ionization efficiencies in the aerodyne aerosol mass spectrometer and aerosol chemical speciation monitor, Aerosol Sci. Technol., 57(10), 981–997, 2023.

Ortega, J., Snider, J. R., Smith, J. N. and Reeves, J. M.: Comparison of aerosol measurement systems during the 2016 airborne ARISTO campaign, Aerosol Sci. Technol., 53(8), 871–885, 2019.

680 Pieber, S. M., El Haddad, I., Slowik, J. G., Canagaratna, M. R., Jayne, J. T., Platt, S. M., Bozzetti, C., Daellenbach, K. R., Fröhlich, R., Vlachou, A., Klein, F., Dommen, J., Miljevic, B., Jiménez, J. L., Worsnop, D. R., Baltensperger, U. and Prévôt, A. S. H.: Inorganic Salt Interference on CO2+ in Aerodyne AMS and ACSM Organic Aerosol Composition Studies, Environ. Sci. Technol., 50(19), 10494–10503, 2016.

Schroder, J. C., Campuzano-Jost, P., Day, D. A., Shah, V., Larson, K., Sommers, J. M., Sullivan, A. P., Campos, T., Reeves, 685 J. M., Hills, A., Hornbrook, R. S., Blake, N. J., Scheuer, E., Guo, H., Fibiger, D. L., McDuffie, E. E., Hayes, P. L., Weber, R. J., Dibb, J. E., Apel, E. C., Jaeglé, L., Brown, S. S., Thornton, J. A. and Jimenez, J. L.: Sources and secondary production of organic aerosols in the northeastern United States during WINTER, J. Geophys. Res., 123(14), 7771–7796, 2018.

Stith, J. L., Ramanathan, V., Cooper, W. A., Roberts, G. C., DeMott, P. J., Carmichael, G., Hatch, C. D., Adhikary, B., Twohy, C. H., Rogers, D. C., Baumgardner, D., Prenni, A. J., Campos, T., Gao, R., Anderson, J. and Feng, Y.: An overview of aircraft 690 observations from the Pacific Dust Experiment campaign, J. Geophys. Res., 114(D5), doi:10.1029/2008jd010924, 2009.

Williams, L. R., Gonzalez, L. A., Peck, J., Trimborn, D., McInnis, J., Farrar, M. R., Moore, K. D., Jayne, J. T., Robinson, W. A., Lewis, D. K., Onasch, T. B., Canagaratna, M. R., Trimborn, A., Timko, M. T., Magoon, G., Deng, R., Tang, D., de la Rosa Blanco, E., Prévôt, A. S. H., Smith, K. A. and Worsnop, D. R.: Characterization of an aerodynamic lens for transmitting particles greater than 1 micrometer in diameter into the Aerodyne aerosol mass spectrometer, Atmos. Meas. Tech., 6(11), 695 3271–3280, 2013.

Xu, W., Croteau, P., Williams, L., Canagaratna, M., Onasch, T., Cross, E., Zhang, X., Robinson, W., Worsnop, D. and Jayne, J.: Laboratory characterization of an aerosol chemical speciation monitor with PM2.5 measurement capability, Aerosol Sci. Technol., 51(1), 69–83, 2017.

Xu, W., Lambe, A., Silva, P., Hu, W., Onasch, T., Williams, L., Croteau, P., Zhang, X., Renbaum-Wolff, L., Fortner, E., 700 Jimenez, J. L., Jayne, J., Worsnop, D. and Canagaratna, M.: Laboratory evaluation of species-dependent relative ionization efficiencies in the Aerodyne Aerosol Mass Spectrometer, Aerosol Sci. Technol., 52(6), 626–641, 2018.

Zhang, Q., Stanier, C. O., Canagaratna, M. R., Jayne, J. T., Worsnop, D. R., Pandis, S. N. and Jimenez, J. L.: Insights into the chemistry of new particle formation and growth events in Pittsburgh based on aerosol mass spectrometry, Environ. Sci. Technol., 38(18), 4797–4809, 2004.

705